

AD-A189 618

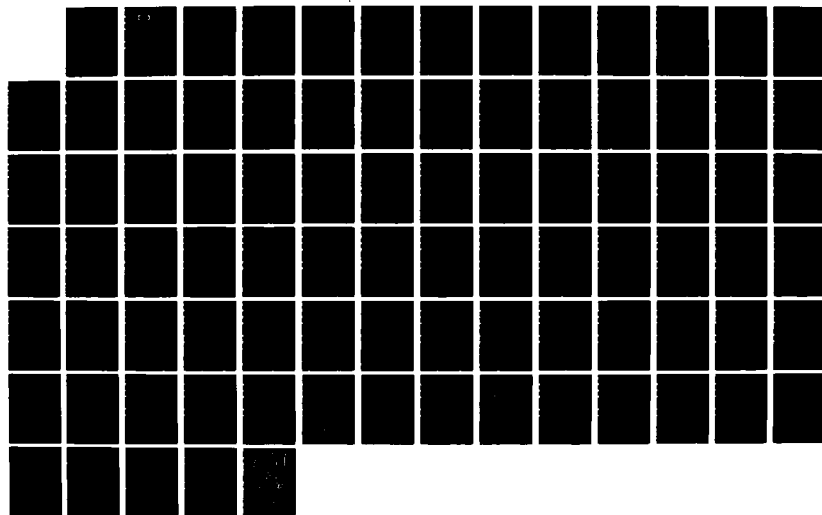
AN EXPERIMENTAL AND THEORETICAL INVESTIGATION OF  
OPTOGALVANIC EFFECTS(U) WISCONSIN UNIV-MADISON DEPT OF  
PHYSICS J E LAWLER DEC 87 ARO-22312 8-PH  
NIPR-ARO-132-86

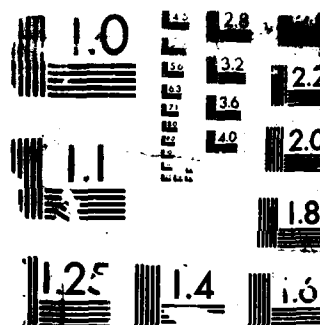
1/1

UNCLASSIFIED

F/G 9/5

NL





RESOLUTION TEST CHART

## DOCUMENTATION PAGE

1a. REPORT SECURITY CLASSIFICATION Unclassified		1b. RESTRICTIVE MARKINGS DTIC FILE COPY	
2a. SECURITY CLASSIFICATION AUTHORITY FEB 02 1988		3. DISTRIBUTION/AVAILABILITY OF REPORT Approved for public release; distribution unlimited.	
2b. DECLASSIFICATION/DOWNGRADING SCHEDULE CD		4. PERFORMING ORGANIZATION REPORT NUMBER PH	
5. MONITORING ORGANIZATION REPORT NUMBER(S) ARO 22312.8-PH		6a. NAME OF PERFORMING ORGANIZATION Department of Physics University of Wisconsin	
6b. OFFICE SYMBOL (if applicable)		7a. NAME OF MONITORING ORGANIZATION U. S. Army Research Office	
6c. ADDRESS (City, State, and ZIP Code) 1150 University Ave. Madison, WI 53706		7b. ADDRESS (City, State, and ZIP Code) P. O. Box 12211 Research Triangle Park, NC 27709-2211	
8a. NAME OF FUNDING/SPONSORING ORGANIZATION U. S. Army Research Office		8b. OFFICE SYMBOL (if applicable)	
9. PROCUREMENT INSTRUMENT IDENTIFICATION NUMBER MIPR ARO 132-86		10. SOURCE OF FUNDING NUMBERS	
8c. ADDRESS (City, State, and ZIP Code) P. O. Box 12211 Research Triangle Park, NC 27709-2211		PROGRAM ELEMENT NO.	PROJECT NO.
		TASK NO.	WORK UNIT ACCESSION NO.
11. TITLE (Include Security Classification) An Experimental and Theoretical Investigation of Optogalvanic Effects			
12. PERSONAL AUTHOR(S) J. B. Lawler			
13a. TYPE OF REPORT Final		13b. TIME COVERED FROM Aug. 84 TO Aug. 87	
14. DATE OF REPORT (Year, Month, Day) Dec. 87		15. PAGE COUNT 85	
16. SUPPLEMENTARY NOTATION The view, opinions and/or findings contained in this report are those of the author(s) and should not be construed as an official Department of the Army position, policy, or decision, unless so designated by other documentation.			
17. COSATI CODES		18. SUBJECT TERMS (Continue on reverse if necessary and identify by block number)	
FIELD	GROUP	SUB-GROUP	
		Cathode Fall Region	
		Optogalvanic Effects	
19. ABSTRACT (Continue on reverse if necessary and identify by block number) Various laser diagnostics are used to study the cathode fall and negative glow regions of a He glow discharge with a cold Al cathode. The electric field and absolute metastable densities are mapped and the gas temperature is measured over a range of current densities from a near normal (173V) to a highly abnormal (600V) cathode fall. These measurements are analyzed to yield the current balance at the cathode surface, the ionization rate in the cathode fall region, and the metastable production rate in the cathode fall and negative glow regions. The experimental results compare favorably with the results of Monte Carlo simulations. The density and temperature of the low energy electron gas in the negative glow is determined by combining information from the experiments and Monte Carlo simulations.			
20. DISTRIBUTION/AVAILABILITY OF ABSTRACT <input type="checkbox"/> UNCLASSIFIED/UNLIMITED <input type="checkbox"/> SAME AS RPT. <input type="checkbox"/> DTIC USERS		21. ABSTRACT SECURITY CLASSIFICATION Unclassified	
22a. NAME OF RESPONSIBLE INDIVIDUAL		22b. TELEPHONE (Include Area Code)	22c. OFFICE SYMBOL

An Experimental and Theoretical Investigation of Optogalvanic Effects

Final Report for the period Aug. 21, 1984 through Aug. 20, 1987

J. E. Lawler

December 1987

U.S. Army Research Office  
 Proposal Number: 22312-PH  
 Grant Numbers: 132-86, 166-84

Dept. of Physics  
 Univ. of Wisconsin  
 Madison, WI 53706



Accession For	
NTIS GRA&I	<input checked="" type="checkbox"/>
DTIC TAB	<input type="checkbox"/>
Unannounced	<input type="checkbox"/>
Justification	
By	
Distribution/	
Availability Codes	
Dist	Avail and/or Special
A-1	

Preface

The preprint entitled "Laser Optogalvanic and Fluorescence Studies of the Cathode Region" forms the body of this report. The paper summarizes more than three years of research on the cathode fall region of glow or diffuse discharges. Although complete self-consistent models of the cathode region are not yet available, we have made significant progress toward this goal. The experimental and theoretical results in the preprint provide a detailed microscopic picture of the cathode region.

List of manuscripts submitted or published under ARO sponsorship during this reporting period, including Journal references.

1. "Spatially Resolved Electric Field Measurements in the Cathode Fall Using Optogalvanic Detection of Rydberg Atoms", D. K. Doughty and J. E. Lawler, Applied Physics Letters 45, 611 (1984).
2. "Optogalvanic Measurements of Gas Temperature in the Cathode Fall", D. K. Doughty, E. A. Den Hartog, and J. E. Lawler, Appl. Phys. Lett. 46, 352 (1985).
3. "Optogalvanic Diagnostics of the Cathode Fall", J. E. Lawler, D. K. Doughty, E. A. Den Hartog, and E. Benck. Invited paper at the 5th I.E.E.E. Pulsed Power Conference at Crystal City, VA, June 10-12 (1985). Published in Digest of Technical Papers 5th IEEE Pulsed Power Conference, edited by P. J. Turchi and M. R. Rose, p371.
4. "Optogalvanic Effects in the Cathode Fall", J. E. Lawler, D. K. Doughty, E. A. Den Hartog, and S. Salih. Invited lecture at the NATO Advanced study Institute on "Radiative Processes in Discharge Plasmas" at Atholl Palace Hotel, Pitlochry, Scotland, June 23-July 5 (1985). Published in Radiative Processes in Discharge Plasmas, edited by J. M. Proud and L. H. Luessen, NATO ASI Series (Plenum Press, New York 1986) Series B, Vol. 149, p525.
5. "Equilibration Distance of Ions in the Cathode Fall", J. E. Lawler, Phys. Rev. A32, 2977 (1985).
6. "An Investigation of the Cathode Fall", D. A. Doughty and J. E. Lawler. Invited paper at the 1986 Materials Research Society Symposium on Plasma Processing, Palo Alto, CA April 15-18 (1986). Published in Materials Research Society Symposium Proceedings Vol. 68, edited by J. W. Coburn, R. A. Gottscho, and D. W. Hess, p141.

7. "Current Balance at the Surface of a Cold Cathode", D. A. Doughty, E. A. Den Hartog, and J. E. Lawler, Phys. Rev. Lett. 58, 2668 (1987).
8. A closely related paper, also entitled "Current Balance at the Surface of a Cold Cathode", by J. E. Lawler, E. A. Den Hartog, and D. A. Doughty was presented at the 6th IEEE Pulsed Power Conference in Crystal City, VA, June 29-July 1, 1987.
9. "Laser Optogalvanic and Fluorescence Studies of the Cathode Region", E. A. Den Hartog, D. A. Doughty, and J. E. Lawler, submitted to Phys. Rev. A.

Scientific personnel supported by this project and degrees awarded during this reporting period.

1. J. E. Lawler is Principal Investigator.
2. D. A. Doughty completed all requirements for his Ph.D. in May, 1987. His thesis title is "Investigation of the D. C. Glow Discharge Using Optogalvanic Spectroscopy". The degree was awarded at the August 1987 commencement exercise. D. A. Doughty received awards from Sigma Xi and the Materials Research Society for his thesis research.
3. E. A. Den Hartog is a graduate student. She has made excellent progress toward a Ph.D. thesis. She is likely to graduate in 1988.
4. E. Benck is a graduate student. He will likely finish in 1988.
5. T. Sommerer is a graduate student. He received summer support for theoretical work.



Laser Optogalvanic and Fluorescence Studies of the Cathode Region

by

E. A. Den Hartog, D. A. Doughty, and J. E. Lawler

Dept. of Physics

University of Wisconsin

Madison, WI 53706

Abstract

Various laser diagnostics are used to study the cathode fall and negative glow regions of a He glow discharge with a cold Al cathode. The electric field and absolute metastable densities are mapped and the gas temperature is measured over a range of current densities from a near normal (173V) to a highly abnormal (600V) cathode fall. These measurements are analyzed to yield the current balance at the cathode surface, the ionization rate in the cathode fall region, and the metastable production rate in the cathode fall and negative glow regions. The experimental results compare favorably with the results of Monte Carlo simulations. The density and temperature of the low energy electron gas in the negative glow is determined by combining information from the experiments and Monte Carlo simulations.

## I. Introduction

There has in recent years been a very substantial effort toward the development of a quantitative microscopic understanding of the cathode region of glow discharges.<sup>1-6</sup> This region is of great practical interest because of its importance in plasma processing and in pulsed power devices. Plasma processing includes applications of glow discharges in ion etching, thin film deposition, and plasma treating of surfaces. The stability of pulsed gas discharge lasers and other pulsed power devices is largely determined by the stability of the cathode fall region.

The cathode region is also of great fundamental interest. The hydrodynamic approximation, which is often very useful in the central region of a discharge, fails in the cathode region. If the local  $E/N$  (electric field to gas density ratio) determines the velocity dependence of the electron distribution function, then the electrons are in hydrodynamic equilibrium.<sup>7</sup> The lack of hydrodynamic equilibrium in the cathode fall region is caused by the large and rapidly changing  $E/N$ , and by the proximity of the electrode. The cathode region includes both the cathode fall and negative glow regions. The negative glow has a high density of low energy electrons and very small electric fields. It also is a nonhydrodynamic region because of a low density of high energy "beam" electrons injected from the cathode fall region. Unfortunately the extensive data base of electron transport coefficients such as drift velocities, diffusion coefficients, and Townsend coefficients is not directly applicable in modelling the cathode region.<sup>8</sup> These coefficients are generally measured in drift tube experiments in which considerable effort is devoted to insuring that the hydrodynamic approximation holds.

Nonequilibrium regions are receiving increased attention from theorist and experimentalist.<sup>9-12</sup> Because of their nonequilibrium nature, electrons in the cathode fall region are often modelled using either a full Boltzmann equation analysis or a Monte Carlo simulation. A somewhat less realistic but much faster approach is based on a model distribution function with position dependent parameters.<sup>13</sup> The spatial dependences of the parameters such as electron density, average velocity, and average energy, are determined by solving moments of the Boltzmann equation which are coupled ordinary differential equations. These approaches might in general be called nonequilibrium fluid models. Single beam and multiple beam models are examples of this general approach.<sup>14,15</sup> This approach is attractive because it is usually easier and faster to solve moments of the Boltzmann equation which are coupled ordinary differential equations than it is to solve the full Boltzmann equation which is a partial differentio-integral equation. The nonequilibrium fluid approach can in principal be made quite realistic if one is sufficiently clever in the design of a model distribution function for the electrons.

A more complete solution will require a calculation of self consistent space charge electric fields. This will involve coupling Poisson's equation and one (or more) moment equation(s) for ions to the moment equations for electrons. Consider a model which includes three moments of the Boltzmann equation for electrons, Poisson's equation, and a single continuity equation for ions. This model requires the simultaneous solution of five coupled first order differential equations. Four natural boundary conditions include: specifying the electron distribution function at the cathode and specifying an electron emission coefficient for ion bombardment of the cathode. The "missing" condition is unfortunately not a boundary condition but rather an

extremum condition. The physically correct solution will maximize the current at fixed voltage or minimize the voltage at fixed current.

The problem described in the preceeding paragraph is obviously quite difficult. It is also incomplete because of the important role played by metastable atoms, and UV or VUV photons in releasing electrons from the cathode. Appropriate balance equations for these neutral particles must also be included in the problem.

A complete solution to the cathode fall problem is beyond the scope of this paper. This paper describes extensive experimental results from recently developed laser optogalvanic diagnostics, and more traditional laser-induced fluorescence and laser absorption diagnostics.<sup>16</sup> These experimental results include electric field maps, gas temperature (density) measurements, and absolute metastable density maps in a He glow discharge over a range of current densities from a near normal cathode fall of 173V to a highly abnormal cathode fall of 600V. These experimental results are analyzed in detail to provide information on electron impact ionization and excitation in the cathode fall and negative glow regions. Monte Carlo simulations of electron avalanches in the cathode region are compared to the experimental results. The Monte Carlo code is based on Boeuf and Marode's variation of the null collision technique for non-uniform fields.<sup>17</sup> The agreement of the Monte Carlo results and the experimentally derived ionization and excitation rates is generally good. Finally the experimental results are combined with Monte Carlo simulations to infer the density and temperature of the low energy electron gas in the negative glow. This unexpected information is largely based on observation of a suppression of the  $2^1S$  metastable density in the negative glow due to metastable spin conversion by low energy electron collisions.

The results of this paper can be viewed in several ways: (1) as a test of our understanding of the key physical processes in the cathode region, (2) as a set of benchmark experiments for further modelling of the cathode region, or (3) as a starting point for more ambitious experiments to study electron emission from the cathode. We plan to make in-situ determinations of the relative importance of, and coefficients for, electron emission due to ion, metastable atom, and UV or VUV photon bombardment of the cathode.

The structure of this paper is as follows. Section II is a description of the experimental apparatus. Sections III and IV are, respectively, a presentation of the electric field and gas density measurements, and an analysis of this data to yield information on ionization in the cathode fall region. The field maps and gas density measurements are combined with an analytic treatment of ion transport in the cathode fall region to determine the current balance, or ratio of ion to electron current at the surface of the cathode. This ratio is found to be 3.3 and is independent of the total discharge current. Section V and VI are respectively, a presentation of the metastable density maps and an analysis of metastable diffusion and kinetics in the cathode fall and negative glow regions. The analysis of the data yields  $2^1\text{S}$  and  $2^3\text{S}$  metastable production rates and a rate for  $2^1\text{S}$  metastable quenching due to low energy electron collisions in the negative glow. Sections VII and VIII are, respectively, a discussion of the Monte Carlo code including electron impact cross sections and a comparison of the Monte Carlo results with the experimental results. Section VIII also includes an analysis of the density and temperature of the low energy electrons in the negative glow. Finally Section IX, includes a summary, some conclusions, as well as speculations on future work.

## II. Experimental Apparatus

Figure 1 is a schematic of the experimental apparatus. The discharge used in these studies is produced between flat circular Al electrodes 3.2 cm in diameter and separated by 0.62 cm. The electrodes are water-cooled to minimize gas heating. The discharge tube is made primarily of glass and stainless steel. Most of the large seals are made with knife edge flanges on Cu gaskets. The only exceptions are the high vacuum epoxy seals around the fused silica brewster windows. A liquid N<sub>2</sub> trapped diffusion pump evacuates the tube to  $2 \times 10^{-8}$  Torr. When no liquid N<sub>2</sub> is in the trap an ion pump maintains the vacuum to prevent oil from back-diffusing into the system. The leak rate into the sealed discharge tube is approximately  $3 \times 10^{-4}$  Torr/day. For discharge operation ultra high purity (0.999999) He is slowly flowed through the system. A capacitive manometer monitors the pressure which is maintained at 3.5 Torr. The He first passes through a cataphoresis discharge to remove any residual contaminants before entering the main discharge tube. Emission spectra reveal only weak Al and H impurity lines. Although He is much less effective at sputtering than heavy inert gases, some sputtering of the Al cathode does occur. We suspect that the slow erosion of the cathode gives rise to both the weak Al and H impurity lines. Many metals absorb hydrogen. The surface of the Al cathode is cleaned in-situ by running an Ar discharge. Argon is very effective at sputtering most metals including Al. A carefully prepared cathode provides discharge V-I characteristics which are stable to a few percent over a period of a month.

Experiments are carried out over a range of discharge current densities from 0.190 mA/cm<sup>2</sup> to 1.50 mA/cm<sup>2</sup>. The low current density corresponds to a near normal cathode fall voltage of 173 V and the high current density corresponds to a highly abnormal cathode fall voltage of 600 V. The discharge

current is spread uniformly across the surface of the electrodes. The absence of significant fringing was verified by segmenting the 3.2 cm diameter cathode into a 1.6 cm diameter disc and a close fitting annulus with an outside diameter of 3.2 cm. Each part of the cathode was maintained at the same potential during operation and the average current density on each was measured. The current density was found to be uniform across the cathode. This measurement is one of the justifications for using one dimensional models of the cathode fall region. The segmented cathode was replaced by a solid cathode after the current density measurements.

The laser used is a  $N_2$  laser pumped dye laser. Several different configurations for the dye laser are used, depending on the specific experiment. The dye laser is tunable over a wavelength range 360-700 nm. Frequency doubling crystals are used to extend this range down to 200 nm. For electric field measurements the laser is frequency doubled in order to excite Rydberg levels from the heavily populated metastable levels. The dye laser is operated with a bandwidth of 0.2 to 0.4  $cm^{-1}$ . The spectral widths of components of Rydberg atom Stark manifolds are often much broader than a few tenths of a  $cm^{-1}$  due to the spatial gradients of the electric field in the cathode fall. We find it unnecessary to reduce the dye laser bandwidth below 0.2  $cm^{-1}$  for electric field measurements using Rydberg atoms. The dye laser bandwidth is reduced to 0.01  $cm^{-1}$  (300 MHz) for measuring the Doppler width of a transition between non-Rydberg levels. The dye laser is operated with a bandwidth of 0.2  $cm^{-1}$  to 0.4  $cm^{-1}$  for laser induced fluorescence studies of the spatial distribution of metastable atoms. The absolute metastable density is provided by an absorption experiment. The pulsed dye laser power must be substantially reduced to avoid saturation in the absorption experiments. We also found it convenient to reduce the dye laser bandwidth to 0.017  $cm^{-1}$ . A

very small instrumental contribution simplifies analysis of the absorption data.

Figure 1 shows all three detection schemes used in these experiments. Optogalvanic detection involves using the boxcar averager to monitor the current through the discharge by observing voltage changes across the 263  $\Omega$  resistor between the cathode and ground. This detection scheme is particularly sensitive in the cathode fall region because optogalvanic effects are naturally amplified by the cathode fall.<sup>18</sup> Optogalvanic detection is essential for observing transitions to Rydberg levels. The fragile Rydberg atoms do not live long enough in order to fluoresce in the visible or UV; they are rapidly collisionally ionized through associative ionization and other mechanisms. The oscillator strengths for transitions from the heavily populated metastable levels to the Rydberg levels are very small and a direct observation of absorption would be extremely difficult. Optogalvanic detection is also used in the Doppler width measurements reported in this work. Optogalvanic detection is not suited to map the metastable density. The efficiency of the optogalvanic effect is strongly position dependent in the cathode region. Laser-induced fluorescence provides the most convenient detection method for mapping the spatial distribution of metastables. The fluorescence is detected with a photomultiplier after passing through an interference filter which blocks much of the spontaneous emission from the discharge and much of the laser light scattered from windows, etc. The least sensitive detection method used in the experiments is direct absorption. This method does provide a convenient absolute calibration for the metastable density maps. The photodiode shown in Fig. 1 is used in absorption experiments.



In order to perform spatially resolved measurements without disturbing laser alignment the discharge is mounted on a precision translation stage. Good spatial resolution is achieved, when necessary, by passing the laser beam through a narrow slit and imaging the slit into the discharge region.

### III. Electric Field and Gas Density Measurements

Space charge electric fields in gas discharges have traditionally been measured using electron beam deflection. A laser induced fluorescence technique for field measurements was recently developed by Moore, Davis, and Gottscho.<sup>19</sup> A laser technique based on optogalvanic detection of Rydberg atoms was recently developed by Doughty, Salih and Lawler.<sup>16,20</sup> Both laser techniques have a number of important advantages over the traditional electron beam deflection technique.<sup>21</sup> The laser techniques are useful at higher pressures and discharge current densities. It is easier to use a spectroscopic technique in a high purity discharge system. The laser techniques are truly nonperturbing when performed with a nanosecond pulsed laser because the field is measured when the atoms or molecules absorb the laser light, and any perturbation to the discharge fields occurs on a longer time scale. Lasers have the potential for making measurements with a few microns spatial resolution and nanosecond temporal resolution. The technique based on Rydberg atoms has broad applicability because all atoms and molecules have Rydberg levels. This technique also has a wide dynamic range because one can choose an appropriate principal quantum number. The Rydberg atom technique has been used to measure fields as small as  $10 \text{ V/cm} \pm 1 \text{ V/cm}$ .<sup>22</sup>

The technique based on optogalvanic detection of Rydberg atoms excited with a single laser is used in this investigation.<sup>16</sup> A technique involving intersecting laser beams for pinpoint field measurements has also been demonstrated.<sup>20</sup> The discharge studied in this experiment is sufficiently one

dimensional that the simpler single laser technique is adequate. In addition to the advantages described in the preceeding paragraph, a Rydberg atom technique offers an advantage in ease of interpretation. The experimental Stark spectra are analyzed by comparing to theoretical Stark maps. Straightforward, ab initio calculations of these Stark maps to 1% accuracy are possible for many atoms. An excellent procedure for calculating the Stark maps is described in detail by Zimmerman, Littman, Kash, and Kleppner.<sup>23</sup> The procedure used in this work is a simplified version of that described by Zimmerman et. al. The main simplification is that we use corrected hydrogenic radial matrix elements instead of performing a numerical integration for radial matrix elements.

A Rydberg atom is an atom with one of its electrons excited to a high lying energy level characterized by a large principal quantum number,  $n$ . As  $n$  increases many atomic properties tend towards those of hydrogen. The energy of Rydberg states is given by the empirical formula,

$$W_{nl} = W_{ion} - \frac{R_0}{(n-\delta_l)^2}, \quad (1)$$

where  $W_{ion}$  is the ionization potential,  $R_0$  is the Rydberg constant,  $l$  is the angular momentum quantum number, and  $\delta_l$  is the quantum defect. This expression describes hydrogenic energy levels for  $\delta_l = 0$ . The quantum defect reflects the degree of interaction of the outer valence electron with the core electrons. For large values of  $l$  the valence electron's orbit is nearly circular, so it does not interact to any significant degree with the core. Consequently, this electron sees essentially a Coulomb potential implying  $\delta_l$  is vanishingly small. Low angular momentum orbits, such as s and p orbits, do penetrate the core,

thus interacting strongly with the charges there. On average, an s orbit will see a net core charge greater than one because of its penetration, so this level will be more tightly bound than the other levels of the same principal quantum number and the quantum defect will be larger. These qualitative descriptions explain why  $\delta_l$  is weakly dependent on n but strongly dependent on l.

Mixing of states with different principal quantum numbers occurs if both the field and principal quantum number are sufficiently large. This is an undesirable complication if one is studying a discharge and simply using Rydberg atoms as a probe. It can usually be avoided by choosing an appropriate, somewhat lower principal number for very high fields. In heavy atoms with large quantum defects it may be necessary to include states, which are nearby at zero field, but have different principal quantum numbers. In He all quantum defects are less than 0.5.

The energy perturbations are calculated by diagonalizing an (n-m) by (n-m) Hamiltonian matrix, where m is the component of angular momentum along the field axis. The basis set is made of eigenfunctions of the unperturbed Hamiltonian. The diagonal matrix elements are the unperturbed energies of the levels as given in Eq. 1. The quantum defect,  $\delta_l$ , can be deduced from Moore's tables of energy levels<sup>24</sup>. The off-diagonal elements vanish except those connecting states for which l differs by one. These matrix elements are approximately the hydrogenic matrix elements given by the expression:

$$\begin{aligned} &\langle n \ l \ m | e \vec{E} \cdot \vec{r} | n \ l-1 \ m \rangle \\ &= (3/2) e E a_0 n \left[ \frac{(n^2 - l^2)(l^2 - m^2)}{4l^2 - 1} \right]^{1/2}, \end{aligned} \quad (2)$$

where  $e$  is the unit charge, and  $a_0$  is the Bohr radius. The dipole matrix elements above must be corrected to account for core penetration effects. A correction factor of order one has been tabulated as a function of quantum defect by Edmonds, et. al.<sup>25</sup>

Figure 2 presents the results of applying the procedure outlined above to the  $n = 11$ ,  $m = 0$ , singlet levels of He. The diagonal elements are determined from the splittings of the  $11^1S$ ,  $11^1P$ ,  $11^1D$ ,  $11^1F$ , and  $11^1G$  levels, whereas the H, I, K, L, M and N levels are approximated as being degenerate with the  $11^1G$  level.<sup>24</sup> A 5% correction is applied to the S-P matrix elements to account for core penetration.<sup>25</sup> Corrections to the other elements are generally less than 1%. Figure 2a is a plot of the energies of the  $m = 0$  states for the  $n = 11$  levels as a function of applied electric field. The energies are the eigenvalues of the diagonalized Hamiltonian. Only ten components appear in this figure since the  $11^1S$  level has a large quantum defect and is  $23 \text{ cm}^{-1}$  below this pattern. This level does not mix strongly with the other  $n = 11$  levels at the fields indicated in the figure. For fields above 200 V/cm the pattern clearly reflects a linear Stark effect.

Figure 2b is a plot of the expected intensity of selected Stark components from Fig. 2a as a function of electric field. Suppose transitions between a low-lying non-Rydberg  $^1S$  level and the  $n = 11$  Rydberg states are driven. With no external electric field, only the  $^1S \rightarrow 11^1P$  transition will be observed. The effect of the field is to mix a fraction of the  $11^1P$  state into each  $n = 11$  state. This fraction is determined by squaring the appropriate element from an eigenvector of the diagonalized Hamiltonian. The fraction is a relative linestrength for a transition to that component of the Stark manifold. The relative linestrengths of the components labeled 1, 3, and 8 are plotted in

Fig. 2b. Such information is useful in determining electric fields in the case where the splittings between individual components are small.

In order to use Rydberg atoms to measure discharge electric fields these states must first be produced (there is no appreciable steady state population in the cathode fall region) and then detected. The narrow bandwidth and high power characteristics of the laser make it an ideal tool to excite atoms from a well populated lower level to a specific Rydberg level. Since the oscillator strength decreases as  $1/n^3$  it is very difficult to directly detect the weak absorption. Laser induced fluorescence from these atoms is also difficult to detect, because in the 1 - 10 Torr pressure regime the Rydberg atoms do not survive long enough to radiate. They are collisionally ionized via collisions with ground state atoms. Associative ionization:



is likely important for Rydberg levels below the ionization limit by more than thermal energies. The absorption of laser radiation produces excess ionization in the discharge and thus produces an optogalvanic effect. An optogalvanic effect is detectable as a perturbation of the discharge current and can in general be either positive (increased current) or negative. Absorption of radiation may in some cases cause a reduction of ionization in the discharge and a decrease in discharge current.<sup>26</sup> Optogalvanic spectroscopy is uniquely suited to the detection of Rydberg atoms in a discharge environment.

The cathode fall region is particularly well suited to optogalvanic detection. If an extra ion-electron pair is introduced into the cathode fall region the electron is accelerated by the field, thus producing additional ionization. This amplification can result in optogalvanic effects in the

cathode fall region that are 100 times more sensitive than optogalvanic effects in the positive column.<sup>18</sup>

If the lower level from which the transition is driven is metastable, the ionization process results in the destruction of the metastable atom. The destruction of atoms in these levels can produce a negative optogalvanic effect since metastables diffusing to the cathode have a large probability of releasing electrons from the cathode. It would seem that this negative optogalvanic effect might cancel the positive optogalvanic effect which is due to the extra electron produced by associative ionization. The time scales for the two signals, however, are vastly different. The diffusion time of the metastables to the cathode can be several hundred microseconds, whereas associative ionization produces a signal in less than 1 microsecond. When produced by a pulsed laser the positive portion of the transient optogalvanic signal is well isolated and can be easily monitored with a boxcar averager.

The critical consideration in measuring discharge electric fields is choosing an appropriate transition to produce the Rydberg atoms. For noble gases in general and He in particular, transitions from the ground state to upper levels are inaccessible with present dye lasers. These gases, however, have metastable levels which are well populated in the discharge. In He, both  $2^1S$  and  $2^3S$  levels are metastable. The  $2^1S$  to  $11^1P$  transition at 321 nm is the most suitable under the conditions of this experiment. Although the  $2^3S$  level has a higher population than the  $2^1S$ , the  $n^3P$  levels have a much higher quantum defect than the  $n^1P$ 's (0.068 and -0.012 respectively)<sup>24</sup>. The larger quantum defect necessitates exciting to a level with a larger  $n$  to observe a linear Stark effect for a given field. The oscillator strength goes as  $1/n^3$  while the number of components increases as  $n$ , so the amount of signal in each component drops as  $1/n^4$ .

Radiation from the dye laser is frequency doubled using a potassium dihydrogen phosphate crystal. The frequency doubled beam is polarized normal to the surface of the cathode so that only  $\Delta m = 0$  transitions are excited. This results in only  $m = 0$  Rydberg states because the lower level is a  $^1S$ . The beam is focussed in the center of the discharge to a strip approximately 0.01 cm wide and 1 cm long parallel to the surface of the electrodes. As the laser is scanned through the Stark manifold, the current is monitored across a 263 $\Omega$  resistor between the cathode and ground. The photogalvanic signal is processed using a boxcar averager, the output of which is plotted on one channel of a two channel chart recorder. Figure 3 includes representative Stark spectra for a range of distances from the cathode. The splittings of adjacent components or the width of the entire Stark manifold are compared to the Stark map of Fig. 2a to determine the local electric field. A relative frequency calibration is obtained by use of an etalon with an accurately determined spacer. Interference fringes are generated and recorded simultaneously with the spectrum.

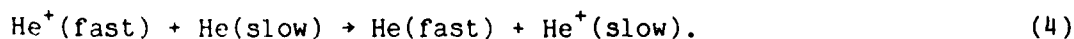
The relative linestrength of Stark components or groups of components is also useful in field measurements.<sup>16</sup> This approach works best at low fields where the linestrengths are strongly dependent on field as indicated in Fig. 2b. The relative linestrengths are equal at high field. In order to determine an electric field from relative linestrengths one must (1) avoid saturation of experimental spectra and (2) establish that the photogalvanic effect is equally efficient on all components. This second condition can be argued on fairly general grounds. Collisions with ground state atoms rapidly mix the populations of the zero field  $n = 11$  levels. The cross section for  $\ell$  mixing of  $n = 11$  Na atoms by collision with ground state He atoms is  $1.85 \times 10^{-3} \text{ \AA}^2$ .<sup>27</sup> It is reasonable to assume that an  $n = 11$  He atom behaves

similarly to an  $n = 11$  Na atom, thus the  $\ell$  mixing rate of approximately  $4 \times 10^9 \text{ sec}^{-1}$  at 3.5 Torr is expected. This mixing rate completely overwhelms radiative decay from the  $11^1\text{P}$  level at a vacuum rate of  $1.4 \times 10^7 \text{ sec}^{-1}$ .<sup>28</sup> Radiation trapping further strengthens the argument by lowering the effective radiative decay rate. A comparison of relative linestrengths must be based on integrated linestrengths because the spectral widths of the Stark components vary across the manifold. The outer components are broadened by the local electric field gradient. The laser probes some finite volume containing a range of field magnitudes. The spectral position of the outer components is most dependent on the field, and hence their width is proportional to the field gradient and the volume probed by the laser.

The results of field measurements as a function of position made at 5 different current densities in 3.5 Torr of He are plotted in Fig. 4. These measurements are based on the splittings of adjacent components and the width of the Stark manifold. The solid lines are linear least square fits to the data. The linear decrease in field magnitude with distance from the cathode is in agreement with the classic picture of the cathode fall region. Close inspection reveals only a very slight negative curvature. This linear behavior persists to quite small fields near the cathode fall-negative glow boundary where the field extrapolates to zero. Direct measurements to rather low fields have been reported by Ganguly et al.<sup>29</sup> The position of the boundary between the cathode fall and negative glow regions can also be confirmed by a qualitative and quantitative change in optogalvanic effects. The excellent agreement between the voltage measured using a digital voltmeter and the voltage determined by integrating the electric field across the cathode fall region indicates that the field measurements are on average accurate to 1%.



It is essential to determine both the electric field and the  $E/N$  throughout the cathode fall region. We found that significant gas heating and a corresponding gas density reduction occurs in the abnormal cathode fall region, even with the water-cooled electrodes in our experiment. Ions carry most of the current in the cathode fall region. The motion of atomic or molecular ions in their parent gas (i.e.  $\text{He}^+$  in He or  $\text{N}_2^+$  in  $\text{N}_2$ ) is limited by symmetric charge exchange



This reaction has a large resonant cross section which is only weakly dependent on energy. It results in a short equilibration distance for ions as discussed in the next section, and a very efficient conversion of electrical energy to heavy particle translational motion and to heat. Examination of the typical  $\text{Nd}_c$  products (gas density times cathode fall thickness) suggests that many of the energetic neutrals scatter before reaching the cathode.

To complement the field measurements in Fig. 4, the gas temperature is measured in the cathode fall region for each of the five current densities of the study. The temperature is found to be constant within an error bar throughout the cathode fall region.

Doppler profiles are obtained by scanning a non-saturating pulsed dye laser through the transition of interest and detecting the resulting optogalvanic signal with a boxcar averager. The beam was focused to a width of 0.06 cm within the cathode fall region. The transition is the  $2^1S$  to  $3^1P$  transition of He at 501.6 nm. The dye laser bandwidth is reduced to 300 MHz by introducing an etalon. Other contributions to the observed lineshape include a natural width of 92 MHz<sup>28</sup>, pressure broadening at 3.5 Torr of 146 MHz<sup>30</sup>, and

Stark broadening on the order of 100 MHz. These contributions are small compared to the Doppler width of 3.66 GHz at 293 K.

The temperature was determined by measuring the full width at half maximum intensity of the line profile. Since the temperature increase is proportional to the power dissipated in the discharge and the Doppler width is proportional to the square root of the temperature, the square of the measured width was plotted as a function of discharge power. If the broadening mechanisms, apart from Doppler broadening, are negligible the resulting extrapolation should indicate a zero power Doppler width which corresponds to ambient gas temperature. The difference between the width calculated at ambient temperature and that indicated by the zero-power extrapolation gives the residual width, which was then subtracted from the measured widths. This correction is less than the size of the error bar. The temperature at each current density was then determined from the width.

Figure 5 is the resulting experimentally derived gas density as a function of discharge power measured at a constant pressure of 3.50 Torr. At the highest power studied, the density is 30% lower than what would be expected assuming ambient temperature. Each data point is determined from 10 Doppler width measurements. These density measurements are combined with the field measurements of Fig. 4 to derive important parameters of the cathode fall region in the next section of this paper.

#### IV. Current Balance at the Cathode Surface

The current balance at the surface of the cathode is the ratio of the ion current to electron current, which is determined from measurements of the electric field and gas density in the cathode fall region and the total discharge current  $J_D$ . The ion current density at the cathode,  $J_+^0$ , is the product of the ion charge density,  $\rho_+$ , and the average ion velocity at the

cathode surface,  $\langle v_z \rangle^0$ . Poisson's equation determines the space charge density in the cathode fall region from the spatial gradient of the electric field. High fields in the cathode fall region result in very high electron velocities and a negligible electron density; the space charge is almost entirely due to the ions.

Ion motion in the cathode fall region is limited by the symmetric charge exchange reaction of Eq. 4. The cold gas or high field approximation is applicable throughout most of the cathode fall region. In this approximation the ion is assumed to start from rest after each charge exchange. It is thus reasonable to argue that the equilibration distance of the ions should be comparable to the mean-free-path for symmetric charge exchange. Each charge exchange collision wipes out all memory of the ion's history. Although the above argument is appealing, two aspects of the cathode fall region complicate the picture. There is a significant field gradient, and new ions are produced throughout the cathode fall region by electron impact ionization.

These complications have both been included in an analytic treatment of ion transport in the cathode fall region.<sup>31</sup> These solutions to the Boltzmann equation for ions will be summarized here. It is convenient to reverse coordinate systems when discussing ions. In most of this paper, parameters are measured and plotted as a function of distance from the cathode. For this discussion of ion transport we choose an origin at the boundary between the cathode fall and negative glow regions, and we let the positive  $z$  axis point toward the cathode. This temporary change in coordinate systems makes the field, ion velocity, and ion flux density positive. The time independent Boltzmann equation is

$$\frac{eE}{m_+} \frac{\partial f}{\partial v_z} + \mathbf{v} \cdot \nabla f = -N\sigma v f + N\sigma \delta(\tilde{v}) \iiint f v dv_z dv_x dv_y + P(z) \delta(\tilde{v}) \quad (5)$$

where  $e$  is a unit charge,  $m_+$  is the ion mass,  $\sigma$  is the charge exchange cross section, and other symbols have their usual meanings. The charge exchange cross section, although weakly energy dependent, is here approximated as independent of energy. The first and second terms on the right hand side of Eq. 5 are Wannier's elegant expression for the collision term due to symmetric charge exchange.<sup>32</sup> The third term is a source term due to electron impact ionization. This source term and the electric field should come from a self-consistent description of the cathode fall region which is beyond the scope of this work. We therefore use a field which increases linearly with distance from the cathode fall-negative glow boundary and replace the ion acceleration  $eE/m_+$  by  $kz$ . The electron impact ionization source term,  $P(z)$ , is known to peak near the cathode fall-negative glow boundary from Monte Carlo simulations by Beouf and Marode, and others.<sup>17</sup> Section VII of this paper describes a determination of  $P(z)$  from Monte Carlo simulation of electron avalanches in the cathode region. A lower limit for the equilibration distance is calculated by assuming that  $P(z)$  describes a plane source at the cathode fall-negative glow boundary. An upper limit for the equilibration distance is calculated by assuming  $P(z)$  describes a uniform source for positive  $z$ . Both limits are derived from the solution to the problem where  $P(z)$  is a plane source  $j\delta(z-z_0)$  and where  $z_0 > 0$ . The distribution function at any positive  $z$  for this source is

$$f_G = j\delta(v_x)\delta(v_y) s(v_z) \{ \exp[-\sigma N(z-z_0)] \otimes \delta(v_z^2 - kz^2 + kz_0^2) +$$

$$(\sigma N/\sqrt{\kappa}) [1-s(v_z^2-kz^2 + kz_0^2)] \exp\{\sigma Nz[\sqrt{1-v_z^2/(kz^2)-1}]/\sqrt{kz^2-v_z^2}\} \quad (6)$$

where  $s(v_z)$  represents a step function and other symbols have their usual meanings. The integral  $\iiint f_G \bar{v} dv_z dv_x dv_y$  is the ion flux density,  $j\bar{z}$ , for all  $z$  greater than  $z_0$ . The flux density must be independent of position by conservation of particles. The integral  $\iiint f_G dv_z dv_x dv_y$  is the ion density which is dependent on position because the ions are accelerating. The distribution function of Eq. 6 for large  $z$  approaches Wannier's equilibrium distribution function<sup>32</sup>

$$f_{eq} = j\delta(v_x)\delta(v_y)[\sigma N/(kz)]s(v_z)\exp[-v_z^2\sigma N/(2kz)]. \quad (7)$$

The lower limit for the equilibration distance of ions in the cathode fall region is determined by letting  $z_0$  approach zero. This limit corresponds to a plane source of ionization at the cathode fall-negative glow boundary. The average velocity in the  $z$  direction for the case where  $z_0$  approaches zero is

$$\langle v_z \rangle = \frac{\iiint f_G v_z dv_z dv_x dv_y}{\iiint f_G dv_z dv_x dv_y} = \frac{1}{\exp(-\sigma Nz)/(\sqrt{\kappa}z) + \pi\sigma N \exp(-\sigma Nz)[I_0(\sigma Nz)+L_0(\sigma Nz)]/(2\sqrt{\kappa})} \quad (8)$$

where  $I_0(z)$  is a modified Bessel function of order 0 and  $L_0(z)$  is a modified Struve function of order 0 as defined and tabulated in Abramowitz and Stegun.<sup>33,34</sup> The average velocity for this case reaches 90% of the equilibrium drift velocity  $\sqrt{2kz/(\pi\sigma N)}$  in 1.7 mean-free paths. If  $z_0 \gg (\sigma N)^{-1}$  then the field changes only slightly in a mean-free-path and the equilibration distance will

be that of the constant field problem,  $0.65/(\sigma N)$ , or two-thirds of a mean-free-path.<sup>31</sup>

The flux density, average velocity, and ion density are plotted in Fig. 6 for the distribution function of Eq. 6 with  $z_0 \approx 0$ . The flux density, plotted in Fig. 6a, must be independent of  $z$  because the source is localized at  $z_0$  near the origin and the system is in steady state. The average velocity, plotted in Fig. 6b, is a steadily increasing function of  $z$  because the field increases linearly with  $z$ . Figure 6c which is a plot of the ratio of the average velocity to the local equilibrium drift velocity  $\sqrt{2kz/(\pi\sigma N)}$ , clearly shows that the nonhydrodynamic behavior is confined to within a few mean-free-paths of the source near the origin. The equilibration distance of 1.7 mean-free-paths required for the average velocity to reach 90% of the local equilibrium drift velocity is read directly from Fig. 6c. A low average velocity near the origin implies a large ion density because their product is the constant flux density. The ion density is plotted in Fig. 6d. The large ion density near the origin is due to inertia. A large fractional change in ion density per mean-free-path is a manifestation of a nonhydrodynamic region. It is because of this large density gradient that a density gradient expansion of the continuity equation is not applicable near the cathode fall-negative glow boundary. The concept of diffusion must also be abandoned with the density gradient expansion. The density gradient expansion and the concept of diffusion are unnecessary because Eq. 6 is an exact solution to the Boltzmann equation. These issues come up again later in this paper when we argue that there is no "diffusion like" ion current across the cathode fall-negative glow boundary.

Equation 6 for  $f_G$  is very slightly different from  $f_3$  as defined in Eq. 7 of Ref.31. The changes make  $f_G$  defined (zero) for positive  $z$  less than  $z_0$ . Thus  $f_G$  corresponds more closely to Arfken's definition of a one-dimensional

Green's function.<sup>35</sup> The distribution function at any positive  $z$  for a linearly increasing field with arbitrary source function is

$$f = \delta(v_x)\delta(v_y)s(v_z) \int_0^{\infty} P(z_0) \{ \exp[-\sigma N(z-z_0)] \}^2 \delta(v_z^2 - kz^2 + kz_0^2) + (\sigma N/\sqrt{k}) [1 - s(v_z^2 - kz^2 + kz_0^2)] \exp\{\sigma Nz[\sqrt{1 - v_z^2/(kz^2)} - 1]\} / \sqrt{kz^2 - v_z^2} \} dz_0. \quad (9)$$

This integral determines a realistic ion distribution function if a source function from a Monte Carlo simulation is used as  $P(z)$ . The objective here is to prove that the average ion velocity is the equilibrium drift velocity in most of the cathode fall region. The true source function as determined in Monte Carlo simulations peaks near the cathode fall-negative glow boundary, and thus is a decreasing function of  $z$  throughout the cathode fall region. The upper limit on the equilibration distance is determined by using a uniform source for all positive  $z$ . The average ion velocity for a linearly increasing field with a uniform source of ions for all positive  $z$  is

$$\langle v_z \rangle = \frac{\iiint f v_z dv_z dv_x dv_y}{\iiint f dv_z dv_x dv_y} = \frac{z}{\exp(-\sigma Nz) \pi \{ I_0(\sigma Nz) + L_0(\sigma Nz) + \sigma Nz [I_1(\sigma Nz) + L_1(\sigma Nz) + 2/\pi] \} / (2\sqrt{k})} \quad (10)$$

where  $I_1(z)$  and  $L_1(z)$  are modified Bessel and modified Struve functions of order one.<sup>33,34</sup> The distance required for the average velocity to reach 90% of the equilibrium drift velocity  $\sqrt{2kz/(\pi\sigma N)}$  is 5.7 mean-free-paths.

The ratio of the thickness of the cathode fall region  $d_c$ , to the mean-free-path for symmetric charge exchange  $(\sigma N)^{-1}$  is typically 50 to 100 for a rare-gas cathode fall. A change in discharge current or pressure changes  $Nd_c$  only slightly, thus the observation

$$\sigma Nd_c \gg 5.7 \quad (11)$$

justifies using an equilibrium ion drift velocity in nearly all of the cathode fall region. The approximation fails only within the first 6 mean-free-paths from the cathode fall-negative glow boundary. The preceeding proof that the ions are in hydrodynamic equilibrium enables us to complete the determination of the current balance at the surface of the cathode.

The drift velocity at the cathode surface for low currents is determined from Helm's precise mobility data.<sup>36</sup> At the high current densities the drift velocity is calculated using the equilibrium expression

$$\langle v_z \rangle^0 = [2eE^0 / (m_+ \pi \sigma N)]^{1/2}, \quad (12)$$

where  $E^0$  is the field at the cathode surface. The symmetric charge exchange cross section,  $\sigma$ , is taken from the calculations of Sinha, Lin, and Bardsley.<sup>37</sup> These calculations agree with Helm's experimentally derived cross sections. The slight energy dependence of  $\sigma$  does not weaken the proof of equilibration, but it is important to use a value of  $\sigma$  that corresponds to the average ion energy at the cathode surface. The average ion energy at the cathode from the equilibrium distribution function of Eq. 7 is

$$\langle m_+ v_z^2 / 2 \rangle^0 = eE^0 / (2N\sigma). \quad (13)$$



A self-consistent average ion energy, and symmetric charge exchange cross section is conveniently determined from a graphical analysis using a plot of  $\sigma$  verses ion energy. The intersection of the  $\sigma$  verses ion energy plot with a hyperbola defined by Eq. 13 and an empirical  $E^0/N$  determines the self-consistent average ion energy and symmetric charge exchange cross section. The uncertainty in  $\langle v_z \rangle^0$  is  $\pm 4\%$  in all cases.

Table I summarizes the analysis of the electric field and gas density measurements to determine the current balance at the cathode surface. The excellent agreement between  $V_{vm}$ , a voltage determined with a digital voltmeter, and  $V_{ef}$ , a voltage determined from integrating the field data, indicates that the field measurements are on the average accurate to 1%. The uncertainty in the ion charge density,  $\rho_+$ , is comparable to the uncertainty in the field measurements. The electron current density at the cathode surface is  $J_D - J_+^0$  where  $J_D$  is the discharge current density. The electron current density has, of course, a larger fractional uncertainty than the ion current density. The dimensionless ratio  $J_+^0/(J_D - J_+^0)$  is the current balance or ratio of the ion current to electron current at the cathode surface. This ratio is of particular interest because it is the number of ions produced in the cathode fall region per (net) electron emitted from the cathode.

#### V. Metastable Density Measurements

The spatial dependence of  $2^1S$  and  $2^3S$  He metastable densities are mapped along the axis of the discharge. The experiment has two parts: 1) laser-induced fluorescence is used to create spatial maps of relative metastable densities and 2) absorption measurements are used to put an absolute scale on the density maps. The absolute density of metastables is modelled in the next section to derive metastable production rates for comparison to Monte Carlo simulations. From the spatial distribution of metastables, and

specifically from the suppression of  $2^1S$  metastables in the negative glow, valuable information is gained about the low energy electrons in the negative glow.

Relative metastable density maps are produced for each of the 5 current densities under study. The laser-induced fluorescence measurements are made using a pulsed  $N_2$  laser pumped dye laser tuned to either the 501.6 nm transition for mapping  $2^1S$  density or the 388.9 nm transition for mapping the  $2^3S$  density. The beam passes through a 250  $\mu m$  slit which was imaged 1:1 into the center of the discharge using a 13 cm focal length cylindrical lens. The laser polarization is along the axis of the discharge. Fluorescence is collected in a direction mutually perpendicular to the laser axis and the axis of the discharge. A lens and slit combination is used to isolate the central portion of the laser-discharge interaction region. This eliminates possible distortion of the spatial map due to metastable populations in the fringes. The lens is masked to cut down on scattered fluorescence which can also distort the map.

Excitation transfer among the  $n = 3$  levels due to collisions with ground state atoms allows the monitoring of fluorescence at a wavelength different from that of the laser.<sup>38</sup> Interference filters are used to isolate 667.8 nm ( $3^1D - 2^1P$ ) radiation when the laser is tuned to 501.6 nm and 706.5 nm ( $3^3S - 2^3P$ ) radiation when the laser is tuned to 388.9 nm. In this way scattered laser light is eliminated from the signal. The fluorescence is detected with a photomultiplier. The entire fluorescence collection system is mounted on the translation stage so it remains fixed with respect to the discharge. The signal is digitized and integrated using a Transiac 2001S transient recorder with a 4100 averaging memory interfaced with an IBM PC.

The laser absorption measurements for determining an absolute scale for the metastable densities are made using the same transitions as the laser-induced fluorescence studies. An etalon is introduced to reduce the laser bandwidth to 500 MHz. The beam passes through a 500  $\mu\text{m}$  slit which is imaged 1:1 into the discharge. Absorption measurements are made at the peak of the spatial density at two current densities. The intensity of the laser is substantially reduced to avoid saturation of the transition. The transmitted laser light is monitored with a photodiode detector. The signal from the detector is processed with a boxcar averager and plotted on a strip-chart recorder as the laser is scanned through the transition. Metastable densities are determined from the integral over frequency of the natural log of the transmittance. Each density is an average of 10 measurements.

Figures 7 and 8 show the results of the metastable density measurements. The density maps have an uncertainty of ~20% in the center of the discharge rising to ~30% near the electrodes.

## VI. Metastable Transport and Kinetics

The transport and kinetics of  $2^1\text{S}$  and  $2^3\text{S}$  metastables in the discharge is modelled using a pair of balance equations which are coupled differential equations:

$$D_s \frac{\partial^2 M_s}{\partial z^2} - \beta M_s^2 - \beta M_s M_t - \gamma M_s N - \kappa n_e M_s + P_s = 0 \quad (14)$$

$$D_t \frac{\partial^2 M_t}{\partial z^2} - \beta M_t^2 - \beta M_s M_t + \kappa n_e M_s + P_t = 0 \quad (15)$$

where:  $M_{s,t}$  = metastable density

$N$  = density of ground state atoms

$n_e$  = density of low energy electrons

$D$  = diffusion coefficient

$P$  = production rate per unit volume

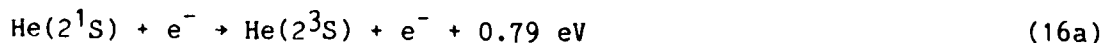
$\gamma$  = rate constant for singlet metastable destruction due to collisions with ground state atoms

$\beta$  = rate constant for destruction of metastables due to metastable-metastable collisions

$\kappa$  = effective rate constant for destruction of singlet metastables due to low energy electron collisions

s and t subscripts indicate singlet and triplet metastables respectively.

The first three terms in each equation are loss terms arising from diffusion and collisions between metastables. There is an additional loss term in the singlet equation due to collisions with ground state He atoms. The marked suppression of singlet metastables in the negative glow (refer to Fig. 7) is due to low energy electron collisions, i.e. the reactions:



These reactions both have large cross sections. Exothermic reaction 16a is a spin exchange, s-wave process with a large cross section for low energy electrons. Endothermic reaction 16b corresponds to a very strong optically allowed transition; it has a large cross section peaking at electron energies roughly three times threshold energy. Reaction 16a dominates the  $2^1\text{S}$  quenching, because 16b must compete with the  $2^1\text{P} \rightarrow 2^1\text{S}$  radiative decay. The

metastable spin conversion reaction 16a is included as the fifth loss term in the singlet equation and a corresponding gain in the triplet equation.

Low energy electrons are confined to the negative glow region due to the high fields in the cathode fall region. The spatial dependence of the low energy electron density,  $n_e$ , is therefore that of a step function; it is zero in the cathode fall region rising sharply at the negative glow boundary to some constant value. The spatial dependence of the production terms is assumed to be a fundamental diffusion mode except at the highest and lowest currents where the fundamental mode is skewed slightly to maintain the peak at the cathode fall-negative glow boundary. The assumption that the production peaks at the boundary is borne out by Monte Carlo simulations discussed later in this paper. Values for  $DN$ ,  $\gamma$  and  $\beta$  are taken from Phelps.<sup>39</sup> The temperature dependence of  $D$  is taken from Buckingham and Dalgarno,<sup>40</sup> that of  $\gamma$  is taken from Allison, Browne and Dalgarno.<sup>41</sup>

The key quantities which are determined in this modelling are the integrated production rates,  $\int P_s dz$  and  $\int P_t dz$ , and the product of the rate constant for metastable spin conversion with the low energy electron density,  $\kappa n_e$ . Values for these key quantities are assumed, the coupled equations are solved for  $M_s(z)$  and  $M_t(z)$ , and a comparison is made to the empirical metastable density maps. Diffusion modes up to tenth order are included in the solutions because of the spatial assymetry introduced by metastable spin conversion. After the comparison with the empirical metastable maps, the values for  $\int P_s dz$ ,  $\int P_t dz$ , and  $\kappa n_e$  are adjusted and the processes iterated until a good fit to the empirical metastable maps is achieved. The value for  $\kappa n_e$  determined in this fashion should be considered an effective rate of metastable spin conversion because it must be modified to include the reverse reaction. The reverse reaction is not negligible if the relative singlet verses triplet

metastable density approaches thermal equilibrium with the low energy electron gas in the negative glow.

Figures 9 and 10 show both the measured and calculated  $2^1S$  and  $2^3S$  densities respectively for one of the current densities. Table II summarizes for all current densities the parameters used in the model such as  $D_S$ ,  $D_T$ ,  $\gamma$ , and  $\beta$  and the key quantities  $\int P_S dz$ ,  $\int P_T dz$ , and  $\kappa n_e$ . The dimensionless ratios  $e \int P_S dz / (J_D - J_+^0)$  and  $e \int P_T dz / (J_D - J_+^0)$ , where  $J_D - J_+^0$  is the empirical electron current density at the cathode, are of particular interest. These dimensionless ratios are the average number of singlet and triplet metastables produced per (net) electron emitted from the cathode.

#### VII. Monte Carlo Simulations

Monte Carlo simulations are now widely used to study the behavior of charged particles in weakly ionized gases. These simulations are not as elegant as a numerical solution of the Boltzmann equation, and they do require considerably more computer time than numerical solutions. The computer time issue is steadily decreasing in significance; all of the simulations described in this work were executed on a personal computer. Monte Carlo simulations are very easy to code, and they can be made quite realistic if sufficient high quality data is available on cross sections including angular distributions for elastic scattering, for excitation, and for ionization. It is straightforward to include almost any amount of detail in a simulation which is justified by the data base of cross sections. Any well defined physical quantity can be determined in a Monte Carlo simulation. Monte Carlo simulations are often used to test numerical solutions of the Boltzmann equation which usually require some approximations. The simulations are also very useful for comparison to experiments.

Monte Carlo simulations are used in this work to study electron avalanches in the cathode fall and negative glow regions. There is no need for Monte Carlo simulations of ion transport in the cathode fall region because we have the exact analytic solutions to the Boltzmann equation for ions as presented in Section IV. The Monte Carlo simulations include the empirical field distributions and gas densities for the cathode fall region as given in Section III. A uniform field of 1.0 V/cm or 10.0 V/cm is assumed for the negative glow region. We suspect that there is actually a reversal of the field direction at the boundary between the cathode fall and negative glow regions. The reversal would produce a potential energy well which holds the low energy electron gas of the negative glow. The reversal would also result in a back diffusion (or drift) toward the anode of ions produced in the negative glow. Unfortunately it is difficult to include a field reversal in the Monte Carlo simulations. However, the actual magnitude and direction of the weak field in the negative glow region has very little effect on excitation and ionization in the negative glow which is produced by high energy beam electrons from the cathode fall region.

The Monte Carlo simulations are three dimensional in the sense that they include angular scattering, but they do not include edge effects due to fringing of the discharge. One dimensional infinite plane parallel geometry is assumed. The most convenient coordinates are  $T$ ,  $\mu$ , and  $z$  where  $T$  is the electron's kinetic energy,  $\mu$  is the cosine of the angle between the electron's velocity and acceleration, and  $z$  is the distance from the cathode. The acceleration  $\bar{a}$  of magnitude  $|eE/m_e|$  is in the positive  $z$  direction. We ask the reader to note that we have returned to our original coordinate system, which was abandoned only during the discussion of ion transport in Section IV. The

quantity  $s$  is a distance along an electron's trajectory between collisions, and  $W$  is electron's potential energy.

Two quantities are conserved while the electron is in free flight between collisions, the transverse kinetic energy  $T^*$  where

$$T^* = T(1-\mu^2) \quad (17)$$

and the total energy  $T + W(z)$ . An electron is launched after a collision with initial conditions  $T_1$ ,  $\mu_1$ , and  $z_1$ . Once a single chosen coordinate is determined immediately before the next collision, such as  $T_c$ ,  $\mu_c$ , or  $z_c$ , the other two coordinates are determined from conservation equations. The change in the chosen coordinate is determined from a pseudo random number in a fashion that reflects the electron's scattering probability along its trajectory. By tracking large numbers of electrons one can determine the same information embodied in a solution to the Boltzmann equation: a phase distribution function and all moments of it. The enormous advantage of a null collision Monte Carlo technique is that it makes it possible to relate the change in the chosen coordinate between collisions to the pseudo random number without performing a numerical integration of scattering probability along the trajectory. Numerical integration is a slow process and is to be avoided if possible.

The null collision technique used in this investigation was developed by Boeuf and Marode for nonuniform fields.<sup>17</sup> The probability density function  $q(s_c)$  is used to describe the differential probability of a collision occurring in a interval  $ds$  about  $s_c$ ,

$$dp = q(s_c)ds = \exp\left\{-\int_0^{s_c} N\sigma[T(s)]ds\right\} N\sigma[T(s_c)]ds. \quad (18)$$

The electron starts with  $s=0$  after the last collision at coordinates  $T_1$ ,  $\mu_1$ ,



$z_1$ . The cross section  $\sigma$  includes elastic, excitation, and ionization scattering. It is obviously very dependent on the electron kinetic energy  $T$ . The exponential in the definition of  $q$  is the probability of the electron surviving without a collision to  $s_c$ , and the remaining factor is the probability of scattering at  $s_c$ . The cumulative distribution function

$$p(s_c) = \int_0^{s_c} dp = \int_0^{s_c} q(s)ds = 1 - \exp\left\{-\int_0^{s_c} N\sigma[T(s)]ds\right\} \quad (19)$$

is a probability of a collision occurring before the electron reaches  $s_c$ . This function should be set equal to a pseudo random number  $r_1$  on the interval from 0 to 1.0 and solved for  $s_c$  to determine  $T_c$  or  $\mu_c$  or  $z_c$  in the Monte Carlo simulation,

$$\int_0^{s_c} N\sigma[T(s)]ds = -\ln(1-r_1) = R. \quad (20)$$

Following Boeuf and Marode we note

$$ds = dz/\mu \quad (21)$$

and

$$adz = dT \quad (22)$$

thus

$$\int_{T_1}^{T_c} \frac{N\sigma(T)}{a\mu} dT = \int_{T_1}^{T_c} \frac{N\sigma(T) \sqrt{T}}{a(T-T^*)^{1/2}} \text{sgn}(\mu) dT = R. \quad (23)$$

Note that the acceleration  $a$ , which is a function of position, must be expressed as a function of  $T$  in order to evaluate this integral. Of course the null collision technique avoids this numerical integration. There is an upper bound,  $B_i$ , of  $N\sigma(T)\sqrt{T}/a$  in the  $i$ th spatial bin defined by the interval  $z_i$  to  $z_{i+1}$ . The integration of Eq. 23 is straightforward if a null scattering process is included, with a cross section chosen such that

$$N[\sigma(T) + \sigma_{\text{null}}(T)] \sqrt{T}/a = B_i \quad (24)$$

throughout the  $i$ th bin from  $z_i$  to  $z_{i+1}$ . Null collisions, when they occur, do not change the electron's velocity. The remaining complications in the integral of Eq. 23 are due to  $\text{sgn}(\mu)$  and to the steps in the integrand caused by  $B_{i-1} \neq B_i \neq B_{i+1} \dots$ . These complications are handled by appropriate branches and loops in the program. First we consider a non-negative  $\mu_1$ . The equation

$$2B_i(\sqrt{T-T^*} - \sqrt{T_1-T^*}) = R \quad (25)$$

is solved, and the solution  $T$  is compared to  $T_{i+1}^b$ , the kinetic energy at the boundary between the  $i$ 'th and  $i$ 'th+1 bin at  $z_{i+1}$ . If  $T$  is less than  $T_{i+1}^b$ , then  $T=T_c$  and a collision occurs in the  $i$ 'th bin. Otherwise the equation

$$2B_{i+1}(\sqrt{T-T^*} - \sqrt{T_{i+1}^b-T^*}) = R - 2B_i(\sqrt{T_{i+1}^b-T^*} - \sqrt{T_1-T^*}) \quad (26)$$

is solved, and the solution  $T$  is compared to  $T_{i+2}^b$ . This procedure is iterated until the bin and the kinetic energy  $T_c$  immediately before the collision is determined. A similar procedure is followed for negative  $\mu_1$  with the additional possibility of the electron reversing direction before colliding.

For example we consider an electron with negative  $\mu$ , but without sufficient longitudinal kinetic energy  $T_1 - T^*$  to reach  $z_i$ . The equation

$$-2B_i(\sqrt{T - T^*} - \sqrt{T_1 - T^*}) = R \quad (27)$$

can be solved for  $T$  only if  $R$  is sufficiently small. A large value of  $R$  implies that the electron passes through the turning point where  $T = T^*$  and  $\mu = 0$ ; thus the equation

$$2B_i(\sqrt{T - T^*} + \sqrt{T_1 - T^*}) = R \quad (28)$$

is solved for  $T$ .

The type of collision is determined by choosing a second pseudo random number  $r_2$  in the interval from 0 to 1.0. The 0 to 1.0 interval is divided into segments, each of length equal to the probability of a particular type of collision at energy  $T_c$ . The cross section  $\sigma$  is a sum of the elastic cross section  $\sigma_{el}$ , the ionization cross section  $\sigma_{ion}$ , and various excitation cross sections. The first segment is of length  $\sigma_{null}(T_c)/[\sigma_{null}(T_c) + \sigma(T_c)]$ , the second is of length  $\sigma_{el}(T_c)/[\sigma_{null}(T_c) + \sigma(T_c)]$ , the third is of length  $\sigma_{ion}(T_c)/[\sigma_{null}(T_c) + \sigma(T_c)]$ , and so on for each excitation cross section. The segment containing  $r_2$  determines the type of collision.

The electron's coordinates  $T_2$  and  $\mu_2$  immediately after the collision must be determined. The procedure is dependent on the type of collision. Null collision, of course, result in  $T_2 = T_c$  and  $\mu_2 = \mu_c$ . The determination of  $T_2$  and  $\mu_2$  for real collisions requires differential cross section. The sources of the cross sections used in the simulation are given during the discussion of  $T_2$  and  $\mu_2$ .

The total and differential elastic scattering cross section for electron impact of He calculated by LaBahn and Callaway are used in the simulations.<sup>42</sup> The coordinate  $\mu_2$  after an elastic collision is calculated from the scattering angle  $\chi$  and the azimuthal scattering angle  $\phi$  using the equation

$$\mu_2 = \mu_c \cos \chi + \sqrt{1 - \mu_c^2} \sin \chi \cos \phi. \quad (29)$$

The scattering angles  $\chi$  and  $\phi$  are determined from two more pseudo random numbers using the equations

$$r_3 = \frac{2\pi}{\sigma_{el}} \int_0^\chi \frac{d\sigma_{el}}{d\Omega} \sin \theta d\theta \quad (30)$$

and

$$r_4 = \phi / 2\pi. \quad (31)$$

Equation 30 can be solved for  $\chi$  by numerical integration of LaBahn and Callaway's differential cross section.<sup>42</sup> Approximations such as

$$\frac{d\sigma_{el}}{d\Omega} = A[1 + g(T_c) \sin^2(\chi/2)]^{-1} \quad (32)$$

are particularly convenient because  $\chi$  can be evaluated without numerical integration. The function  $g(T_c)$  is roughly quadratic in  $T_c$ . The kinetic energy after the collision is

$$T_2 = T_c [1 - (2m_e/m_o)(1 - \cos \chi)], \quad (33)$$

where  $m_0$  is the atom mass.

The analytic expressions given by Alkhazov for excitation cross sections are used in the simulations.<sup>43</sup> Excitation of  $n=2$  through  $n=5$  singlet and triplet s and p levels is included in the simulation. Excitation of the  $n=3$  through  $n=5$  singlet and triplet d levels is also included. There is very little experimental or theoretical information on differential excitation cross sections for electrons on He. Thus we use an isotropic scattering approximation for excitation,

$$\mu_2 = 2r_3 - 1.0 . \quad (34)$$

The kinetic energy immediately after a excitation collision is

$$T_2 = T_c - W_{exc} \quad (35)$$

where  $W_{exc}$  is the appropriate excitation energy. Recoil is neglected in this approximation.

A fraction of the atoms excited to the 3p levels and above are associatively ionized. An accurate determination of the fraction requires accurate associative ionization cross sections, cross sections for excitation transfer due to ground state atom collisions, and radiative decay rates. On the basis of what information is available we estimate that 25% of the atoms in the 3p levels and above are associatively ionized at 3.5 Torr.<sup>28,38</sup> The electrons released in associative ionization contribute to the avalanche, they are assumed to have an initial kinetic energy of 1.0 eV and an isotropic angular distribution. The remaining 75% of the atoms excited to the 3p and higher triplet levels, and all of the atoms excited to the  $3^3S$  and  $2^3P$  levels are assumed to radiate to the  $2^3S$  metastable level. This cascade contribution

is combined with direct excitation of the  $2^3S$  level to determine the total production rate for  $2^3S$  metastables. The total production rate for  $2^1S$  metastables includes direct excitation and a cascade contribution of 19% of the excitation to the  $3p$  and higher singlet levels. The total production rate for the  $2^1P$  resonant level includes direct excitation and a cascade contribution of all of the  $3^1S$  excitation and 56% of the excitation to the  $3p$  and higher singlet levels. These assumptions are based on a significant  $\lambda$  mixing of  $3p$  and higher level populations due to collision with ground state atoms.

In a vacuum nearly all of the atoms excited to the  $2^1P$  resonant level decay to the ground state via VUV emission. Radiation trapping reduces the effective decay rate to  $1.3 \times 10^6 \text{sec}^{-1}$ , which is comparable to the vacuum decay rate of  $1.98 \times 10^6 \text{sec}^{-1}$  for the  $2^1P \rightarrow 2^1S$  infrared branch at  $2\mu\text{m}$ .<sup>28</sup> However the  $2^1P \rightarrow 2^1S$  branch is also trapped in the cathode fall region of our discharge experiments, thus we do not include any of the  $2^1P$  excitation in calculating a total production rate for  $2^1S$  metastables. This approximation is not completely satisfactory because the  $2^1P \rightarrow 2^1S$  branch is not highly trapped in the negative glow where the  $2^1S$  density is suppressed by low energy electron collision. The  $2^1P$  level is feeding population to the  $2^1S$  level through a collisional-radiative coupling, and the  $2^1S$  level is feeding population to the  $2^3S$  through a collisional coupling. The net result is that the Monte Carlo simulation produces a metastable production rate which is somewhat lower than the empirical rate.

The analytic expression by Alkhazov for the total ionization cross section is used in the simulation.<sup>43</sup> Alkhazov also provides an analytic expression for the differential cross section with respect to energy.<sup>43</sup> The kinetic energy of the outgoing scattered electrons is determined from a pseudo random number using the expression,

$$r_3 = \frac{1}{\sigma_{ion}} \int_0^{T_2} \frac{d\sigma_{ion}}{dT} dT. \quad (36)$$

The outgoing ejected electron has kinetic energy

$$T_2' = T_c - T_2 - W_{ion} \quad (37)$$

where  $W_{ion}$  is the ionization potential. The coordinates  $\mu_2$  and  $\mu_2'$  are determined one of two ways.

The first simulations assumed isotropic angular distributions for both outgoing electrons in an ionizing collision. Some of the results based on the isotropic angular distribution for ionizing collisions were presented in a recent Phys. Rev. Letter.<sup>44</sup> The first simulations predicted a current balance in good agreement with experiment in a near normal cathode fall region, but predicted too much ionization in a highly abnormal cathode fall region. The  $E/N$  reaches 3000Td in the abnormal cathode fall region, thus the inelastic processes are resulting in forward peaked angular scattering distributions. Numerical solutions of the Boltzmann equation for electrons have traditionally assumed isotropic angular distributions for inelastic collisions. Recent work by Phelps and Pitchford explores the effect of anisotropic inelastic scattering at very high  $E/N$  in  $N_2$ .<sup>45</sup>

Our second simulations use the same assumptions used by Boeuf and Marode: (1) the incident, scattered, and ejected electron velocities are coplanar, and (2) the scattered and ejected electron velocities are perpendicular.<sup>17</sup> These assumptions result in

$$\cos \chi = \sqrt{T_2 / (T_c - W_{ion})} \quad (38)$$

and

$$\cos \chi' = \sqrt{T_2' / (T_c - W_{ion})} . \quad (39)$$

The azimuthal scattering angle  $\phi$  is determined by a pseudo random number as in Eq. 31. Equation 29 is used to determine  $\mu_2$ . The coordinate  $\mu_2'$  is calculated using

$$\mu_2' = \mu_c \cos \chi' - \sqrt{1 - \mu_c^2} \sin \chi' \cos \phi. \quad (40)$$

The justification for this angular distribution is not strong, but it does represent a reasonable attempt to introduce anisotropic scattering in ionizing collisions.

The details of the electron interactions with the cathode and anode must be specified. The kinetic energy of electrons emitted from the cathode is assumed to be 5.0 eV and they are assumed to have a random angular distribution in the forward direction. The use of a more realistic energy distribution for electrons emitted at the cathode does not affect ionization or excitation in the Monte Carlo simulations. Some electrons are reflected back to the cathode by elastic scattering from He atoms before they suffer an inelastic collision. Electrons do not have sufficient total energy to reach the cathode after an inelastic collision. The percentage of the gross electron emission which is back scattered to the cathode varies from 19% at the lowest current density (a near normal cathode fall) to 3.6% at the highest current density (a highly abnormal cathode fall). All Monte Carlo results are presented in terms of net electron emission from the cathode. The Monte Carlo simulation assumes no reflection from the anode, each electron is absorbed immediately when it reaches the anode. This approximation will cause the Monte Carlo simulation to



predict excitation and ionization rates in the negative glow which are lower than in experiment. The discordance is significant only in the case of the highly abnormal glow discharge at  $1.50 \text{ mA/cm}^2$ .

Figure 11 includes Monte Carlo histograms giving the number of ionization and excitation events per (net) electron emitted from the cathode as a function of distance from the cathode. The results of Fig. 11 are based on the anisotropic angular distribution for ionizing collisions. These histograms are for field distributions and gas densities corresponding to  $0.519 \text{ mA/cm}^2$ . The spatial dependence of the ionization and excitation rates are all described by a roughly symmetric function which peaks near the cathode fall-negative glow boundary. The simulations show that the "beam" electrons in He penetrate beyond the cathode fall-negative glow boundary by a distance comparable to  $d_c$ , the thickness of the high field cathode fall region. The penetration distance will scale as the inverse of the gas density in a fashion similar to  $d_c$ . The  $2^3\text{S}$  metastable excitation has the most asymmetric spatial dependence; it is stronger in the negative glow than in cathode fall region. This is explained by the sharp peak just above threshold in the energy dependence of triplet excitation cross sections. The asymmetry in the empirical maps of the  $2^3\text{S}$  metastable density is due in part to the spatial dependence of triplet excitation. The spatial dependences of excitation and ionization at other discharge current densities are similar. The results of Monte Carlo simulations for all five current densities are presented in Tables III and IV. The Table III results are based on the isotropic angular distribution for ionizing collisions, and those of Table IV are based on the anisotropic angular distribution for ionizing collisions.

The absolute accuracy of the Monte Carlo simulations must be estimated in order to compare the simulations to experiment. Statistical uncertainty is not large because several thousand complete avalanches were simulated for each of the five discharge currents. Alkhazovs' analytic expressions for the He cross sections are based on theoretical and experimental work by many groups.<sup>43</sup> He estimates that the uncertainty is  $\pm 25\%$  at low energy, and  $\pm 5\%$  at high energy where a Born approximation is reliable. We believe his uncertainties are reasonable and we estimate that the Monte Carlo results have an uncertainty of  $\pm 25\%$ .

#### VIII. Comparison of Experimental Results and Monte Carlo Simulations

The first comparison of experimental results to Monte Carlo simulations involves the current balance at the cathode. This dimensionless quantity is the ratio of ion to electron current at the cathode. Figure 12 is a plot of the ratio versus total discharge current density. The experimental measurements are points with uncertainties which are discussed in Section IV. The dotted line is the same ratio determined from Monte Carlo simulations using the isotropic angular distribution for ionizing collisions. The calculations represented by the dotted line were included in a recent Phys. Rev. Letter.<sup>44</sup> The solid line is the ratio as determined from Monte Carlo simulations using the anisotropic angular distribution for ionizing collisions. All Monte Carlo simulations include the same anisotropic elastic scattering. Clearly the assumption of isotropic inelastic scattering is beginning to fail in the highly abnormal cathode fall region where  $E/N$  reaches 3000 Td.

One of the key issues in interpreting the Monte Carlo results is whether or not one should include any of the ionization produced in the negative glow when computing the ratio of the ion to electron current at the cathode. We maintained in a recent Phys. Rev. Letter, and we continue to maintain that

essentially none of the ionization produced in the negative glow contributes to the ion current at the cathode.<sup>44</sup> The ratio of the ion to electron current at the cathode is computed by summing ionization in spatial bins of a Monte Carlo histogram such as Fig. 11. The sum includes spatial bins from the cathode to a distance  $d_c$  from the cathode where the cathode fall - negative glow boundary occurs. The justification for neglecting any "diffusion" of ions across the boundary is postponed until after a discussion of the negative glow.

The current balance from the Monte Carlo simulations includes direct electron impact ionization and associative ionization due to collisions between highly excited and ground state He atoms. Ionization from collisions between pairs of metastable atoms is not included, but it is a small ( $\leq 10\%$ ) contribution to the current balance from the Monte Carlo simulations.

The current balance, typically 3.3, is lower than we first expected. It is also surprisingly independent of total discharge current. The greater electric field and thickness in the cathode fall region at high current are offset by a gas density reduction due to heating. The net result is that on average an electron produces the same amount of ionization in the cathode fall region at low and high discharge currents. It is not yet possible to say whether a current balance of 3.3 is typical: for only He, for inert gases, or for many gases.

The second comparison involves the number of metastable atoms produced in the cathode fall and negative glow regions per (net) electron emitted from the cathode. The experimental measurements are plotted as points in Fig. 13. The empirical metastable production in units of  $\text{cm}^{-2} \text{sec}^{-1}$  is divided by the empirical electron flux density at the cathode  $(J_D - J_+^0)/e$ . The error bars reflect only uncertainties in the metastable density measurements as discussed in Section V. The solid line of Fig. 13 is the result of Monte Carlo

simulations using the anisotropic angular distribution for ionizing collisions. The  $2^1S$  production plotted in Fig. 13a shows excellent agreement between experiment and the Monte Carlo simulations except at  $0.190 \text{ mA/cm}^2$ . The discordance in the near normal glow discharge at  $0.190 \text{ mA/cm}^2$  is in part due to the neglect of the  $2^1P \rightarrow 2^1S$  cascade contribution in Monte Carlo determinations of  $2^1S$  production. At low current densities the  $2^1P \rightarrow 2^1S$  radiation is not completely trapped. The experimental  $2^3S$  production plotted in Fig. 13b is somewhat higher than that predicted by the Monte Carlo simulations. The total  $2^1S$  and  $2^3S$  metastable production plotted in Fig. 13c is also somewhat higher than that predicted by the Monte Carlo simulations. At least two effects are responsible. The experimental  $2^3S$  production and the total metastable production are enhanced by a collisional-radiative coupling in the negative glow of  $2^1P$  population to the  $2^1S$  and indirectly to the  $2^3S$ . Some of the  $2^1P$  production results in metastable production. The disagreement in the highly abnormal glow discharge of  $1.50 \text{ mA/cm}^2$  is in part due to the assumption of no electron reflection from the anode. The Monte Carlo results summarized in Table IV show a very high average kinetic energy ( $>100 \text{ eV}$ ) for electrons hitting the anode in the highly abnormal glow discharge. Some of these electrons should be reflected at the anode. The reflection from the anode will increase excitation and ionization in the negative glow and improve agreement on metastable production between the experiment and Monte Carlo simulations. The reflection will not significantly change the current balance because few of the reflected electrons will return to the cathode fall region and produce ionization.

Figure 13c shows typically 3 metastable atoms produced per net electron emitted from the cathode. This number can be used to estimate the importance of metastable bombardment in electron emission from a cold cathode. If 50% of

the metastables diffuse back to the cathode, and if the electron emission coefficient is 0.5, then the metastables could be responsible for 75% of the electron emission from the cathode.<sup>46</sup>

The overall power balance in the discharge is of considerable interest. The power input to the discharge is very accurately determined from the discharge voltage  $V_{vm}$  and current density  $J_D$ . The power is dissipated primarily by ion transport in the cathode fall region. Ionization (25 eV/event) and excitation (~21 eV/event) are significant but less important than ion transport. The other major power dissipation mechanism is due to energetic electrons hitting the anode.

The amount of power dissipated by each of the four mechanisms is determined using the Monte Carlo results and compared to the input power. The Monte Carlo results based on the anisotropic angular distribution for ionizing collisions are used. The empirical total discharge current density must also be used in analyzing the power balance because the Monte Carlo results are all per (net) electron emitted from the cathode. A simple analytic model of ion transport in the cathode fall region shows that it consumes very nearly 60% of the power dissipated. Let  $H_{it}$  be the power per unit area dissipated by ion transport. The linear variation of electric field and the equilibrium charge exchange drift velocity indicate that

$$H_{it} = \int_0^{d_c} J_+ E dz = \int_0^{d_c} J_+^0 \sqrt{(d_c - z)/d_c} E^0 (d_c - z)/d_c dz =$$

$$J_+^0 E^0 d_c 0.4 = J_+^0 V_{vm} 0.8 = J_D V_{vm} (0.8 J_+^0 / J_D) \quad (41)$$

The ratio of the ion current density at the cathode  $J_+^0$  to the total discharge current density  $J_D$  is approximately 0.75, this ratio is simply related to the current balance at the cathode  $J_+^0 / (J_D - J_+^0)$  as determined in the Monte Carlo

simulations. Nearly 60% of the input power is dissipated by ion transport at all discharge current densities.

The power per unit area dissipated in ionization (25 eV/event) and excitation (21 eV/event) is proportional to the electron current density at the cathode and the number of direct ionization and total excitation events per (net) electron emitted from the cathode. Associative ionization is here included with total singlet plus triplet excitation. The expressions are

$$H_{ion} = (25\text{eV})(J_D/e)[(J_D - J_+^0)/J_D] \text{ (direct ionization events/electron)} \quad (42)$$

and

$$H_{exc} = (21\text{eV})(J_D/e)[(J_D - J_+^0)/J_D] \text{ (total excitation events/electron)}. \quad (43)$$

The ratio of electron current density at the cathode ( $J_D - J_+^0$ ) to the discharge current density  $J_D$  is simply related to the current balance as determined in the Monte Carlo simulations.

The power dissipated in the anode per unit area is

$$H_{an} = (J_D/e)[(J_D - J_+^0)/J_D] (1 + \text{total ionization events/electron}) \langle T_{an} \rangle \quad (44)$$

where  $\langle T_{an} \rangle$  is the average kinetic energy of electrons striking the anode. Again all of the quantities are from the Monte Carlo simulations using the anisotropic angular distribution for ionizing collisions except for the empirical total discharge current density  $J_D$ . The results of the power balance comparison are summarized in Table V. The power balance is quantitatively understood. The second to last row is the total power dissipated per unit area as determined from the Monte Carlo simulations. The last row is the empirical

input power per unit area. The excellent agreement between the last two rows can be interpreted as additional confirmation that the current balance is correct.

The considerable and detailed experimental and theoretical information on the He discharge system described in this work enables us to analyze the negative glow. The negative glow region starts a distance  $d_c$  from the cathode where the cathode fall field extrapolates to zero. It extends to the anode in our discharge cell. The separation of the electrodes was chosen so that no positive column would form. The negative glow region is characterized by extremely small electric fields and a high density  $n_e$  of low energy electrons at temperature  $T_e$ . These low energy electrons are not described in the Monte Carlo simulations. Results from the Monte Carlo simulations such as  $\langle T_{an} \rangle$ , the average energy of electrons striking the anode, are for the high energy beam electrons. The low energy electrons are, as we shall show, trapped in a potential energy well. Monte Carlo simulations are not well suited for describing trapped particles.

The analysis of each empirical singlet metastable map as described in Section VI produced an effective rate  $\kappa n_e$  for metastable spin conversion due to low energy electrons in the negative glow. This process was discovered by Phelps and the rate constant  $\kappa_m$  was measured for room temperature ( $k_B T_e = 0.025$  eV) electrons.<sup>39</sup> The dependence of this rate constant on electron temperature is  $(T_e)^{-1/2}$  because the cross section scales roughly as the inverse of the electron energy.<sup>47</sup> Although we do not a priori know the temperature of the low energy electrons in the negative glow, it is relatively easy to put some limits on it. Surely the temperature of the low energy electrons must be greater than gas temperature. An upper limit on the electron temperature is determined by noting that the exothermic metastable spin conversion reaction

depletes the singlets, but only until the relative singlet versus triplet metastable density comes into thermal equilibrium with the low energy electron gas. Thus the empirical ratio  $M_S/M_t$  in the negative glow must be greater than or equal to  $(1/3)\exp(-0.79/k_B T_e)$ . These limits on  $T_e$  and knowledge of  $\kappa n_e$  determine a range of possible electron temperatures and a corresponding electron density for each temperature as given by the expression

$$\kappa n_e = n_e [\kappa_m \sqrt{0.025 \text{ eV} / k_B T_e} - (M_t / 3M_S) \kappa_m \sqrt{0.025 \text{ eV} / k_B T_e} \exp(-0.79 \text{ eV} / k_B T_e)]. \quad (45)$$

This expression is represented by the bold solid lines of Fig. 14.

The rather high densities of low energy electrons suggests the existence of a potential energy well for electrons, and suggests a simple model for the negative glow. (Without a potential energy well the diffusion current of electrons to the anode would be by far too large.) The negative glow in these experiments can be thought of as a plasma in which ion-electron pairs are produced by beam electrons from the cathode fall region and lost by a process analogous to ambipolar diffusion to the anode. The analogy to ambipolar diffusion is not perfect because the electron flux density on the anode must be larger than the ion flux density on the anode by  $J_D/e$ . The loss rate of low energy electrons should be approximately  $(1/2) \mu_+ k_B T_e (\pi/2 d_{ng})^2 / e$  where  $\mu_+$  is the low field ion mobility and  $d_{ng}$  is the thickness of the negative glow. The factor of  $1/2$  is due to the fact that the negative glow is assymmetric, the low energy electrons cannot diffuse against the cathode field. The rate in the negative glow of ionization per unit volume  $\langle P \rangle$  can be determined from the Monte Carlo simulations of Table IV. The rate  $\langle P \rangle$  is a spatially averaged quantity  $(\int_{d_c}^{d_c + d_{ng}} P dz) / d_{ng}$ . Inclusion of some electron reflection from the



anode will increase  $\langle P \rangle$ , but at most by a factor of two and only in the highly abnormal glow discharge at  $1.50 \text{ mA/cm}^2$ . This model provides a second relation between the density  $n_e$  and temperature  $T_e$  of the low energy electrons in the negative glow

$$\langle P \rangle = n_e \frac{1}{2} \mu_+ k_B T_e (\pi/2 d_{ng})^2 / e . \quad (46)$$

This expression is represented by the light solid lines of Fig. 14. The intersection of the light and bold lines determines the density and temperature of the low energy electrons in the negative glow.

This simple model neglects recombination. We do observe  $\text{He}_2$  molecular emission bands from the negative glow. These bands are conclusive evidence that some recombination occurs. The inclusion of recombination in Eq. (46) will modify the low temperature, high density portion of the balance equation which is plotted as a light solid line in Fig. 14. Recombination will not significantly change the intersection point. The importance of recombination is assessed by substituting the gas density and the density and temperature of the low energy electrons as determined from the simple model into the known He recombination rate.<sup>48</sup> Recombination is at most 4% of the diffusion loss rate  $(1/2)\mu_+ k_B T_e (\pi/2 d_{ng})^2 / e$ .

The occurrence of the intersection on the steep portion of the plots of Eq. 45 is an indication that the metastable spin conversion reaction 16a is proceeding to equilibrium. The relative density of the singlet and triplet metastable is in Boltzmann equilibrium with the low energy, high density electrons in the negative glow. Under such conditions the empirical ratio of singlet to triplet metastables is providing the temperature of the negative glow electrons. The accuracy of this determination of the electron temperature

in the negative glow is not easy to assess. We estimate that the uncertainty of the temperature and density of the negative glow electrons determined in Fig. 14 is no worse than  $\pm 50\%$ . This completes the model of the negative glow.

The justification for ignoring ionization produced in the negative glow when using the Monte Carlo simulations to determine the current balance at the cathode is now obvious. The field direction reverses a distance  $d_c$  from the cathode at the boundary between the cathode fall and negative glow regions. The field has a magnitude on the order of one V/cm in the negative glow. Ions produced in the negative glow drift in a process analogous to ambipolar diffusion toward the anode in the weak field of the negative glow.

The remaining issue is how the ion density of a few  $\times 10^9 \text{ cm}^{-3}$  in the cathode fall joins smoothly to the ion density of  $> 10^{11} \text{ cm}^{-3}$  in the negative glow. One at first might suggest that there will be a large diffusion of ions toward the cathode across the cathode fall-negative glow boundary. This does not occur. Furthermore diffusion is not a valid concept within a few ion mean-free-paths of the cathode fall-negative glow boundary. Diffusion is an intrinsically hydrodynamic concept; it implies a density gradient expansion of a continuity equation. The region, within six mean-free-paths for symmetric charge exchange, from the cathode fall-negative glow boundary is a non-equilibrium region even for ions as shown in Section IV of this paper. The solutions to the Boltzmann equation for ions given in Section IV have a diverging ion density at the boundary. This divergence is a result of the cold gas approximation for the ion production term and for charge exchange collision term used in the Boltzmann equation. The divergence is unphysical, but it is essential to note that large ion density gradients at the cathode fall-negative glow boundary are built in to the exact solution to the Boltzmann equation for ions. There is no theoretical difficulty in smoothly joining the uniform (few

$\times 10^9 \text{cm}^{-3}$ ) ion density of the cathode fall region to a much higher ( $>10^{11} \text{cm}^{-3}$ ) ion density of the negative glow. A physically reasonable source term for electron impact ionization, such as those given by a Monte Carlo simulation for electrons peaks near the cathode fall-negative glow boundary. When such a source term is combined with the Green's function for ions as in Eq. 9 the sharp ion density gradient at the cathode fall-negative glow boundary appears naturally.

#### IX. Summary, Conclusions, and Future Work

Various laser diagnostics are used to study the cathode fall and negative glow regions of a He glow discharge. The water-cooled Al cathode is operated over a range of current densities from a near normal cathode fall of 173V to a highly abnormal cathode fall of 600V. Optogalvanic detection of Rydberg atoms is used to map the electric field in the cathode fall region. The Doppler width of a transition between non-Rydberg levels is used to measure the gas temperature. The gas density is significantly reduced in the abnormal glow discharge due to ion charge exchange heating. Electric field maps and gas density measurements are combined with an analytic treatment of ion transport in the cathode fall region to determine the current balance or ratio of ion to electron current at the cathode. This current balance is 3.3 and is nearly independent of total discharge current. The densities of He  $2^1\text{S}$  and  $2^3\text{S}$  metastables are mapped using laser-induced fluorescence and laser absorption spectroscopy for absolute calibration. An analysis of the metastable maps provides absolute metastable production rates in the cathode fall and negative glow regions and provides a constraint on the density and temperature of the low energy electrons in the negative glow. The constraint arises from our observation of a suppression of the  $2^1\text{S}$  metastable density in the negative

glow. This suppression is due to metastable spin conversion by low energy electron collisions in the negative glow.

The empirical current balance at the cathode surface and the metastable production rates are compared to theoretical results from Monte Carlo simulations of electron avalanches. A Monte Carlo code, based on the null collision technique for nonuniform fields as developed by Boeuf and Marode, is used to simulate electron avalanches. The agreement between the empirical current balance and the result of Monte Carlo simulations is good. The inclusion of an anisotropic angular distribution for ionizing collisions results in excellent agreement, even in the highly abnormal cathode fall region where  $E/N$  reaches 3000 Td. The agreement between the empirical metastable production rates and the results of Monte Carlo simulations is good.

The high density of low energy electrons in the negative glow suggests a simple model for the negative glow and suggests the existence of field reversal at the boundary between the cathode fall and negative glow regions. The empirical constraint on the density and temperature of the low energy electrons in the negative glow is combined with an ionization rate predicted by Monte Carlo simulations to determine the density and temperature of the low energy electrons.

The comparisons of the empirical results and results from Monte Carlo simulations lead us to conclude that excitation and ionization, as embodied in the current balance, are quantitatively understood in the cold cathode He discharge. The power balance is also quantitatively understood. We conclude that the vast majority of ions striking the cathode are produced in the cathode fall region. There is no significant "diffusion like" ion current at the boundary between the cathode fall and negative glow regions. Diffusion is not even an applicable concept because of the lack of hydrodynamic equilibrium

within a few ion mean-free-paths of the cathode fall-negative glow boundary. Our analytic nonequilibrium solutions to the Boltzmann equation for ions in the cathode fall region correctly describes the steep increase in ion density at the cathode fall-negative glow boundary.

The conclusion that ions reaching the cathode surface are produced in the high field cathode fall region is generally valid. A Bohm presheath, if it existed, could preaccelerate ions before they reach the cathode fall-negative glow boundary. Symmetric charge exchange will prevent the development of any structure analogous to a Bohm presheath in the negative glow. It is premature to conclude that the current balance of 3.3 is typical for gases other than He. We can conclude that the experimental and theoretical techniques used in this investigation are broadly applicable.

A quantitative microscopic picture of the cathode fall and negative glow regions is emerging but major challenges remain. A major experimental challenge is to measure the relative importance of, and coefficients for, electron emission from the cathode due to ion, metastable atom, and VUV photon bombardment. The measurements should be done in-situ with a relatively nonperturbing spectroscopic diagnostic. We believe that the spatial and temporal characteristics of carefully chosen optogalvanic effects will provide this information on electron emission. A convincing and fully self-consistent analysis of the optogalvanic effect will likely be difficult. Another experimental challenge is to perform independent measurements of the density and temperature of the low energy electrons in the negative glow region. Again, it should be possible to make the measurements with a relatively nonperturbing spectroscopic diagnostic. On the theoretical side there are many challenges. The ultimate goal is to develop relatively simple, efficient models which provide fully self-consistent fields. The models must also have good microscopic detail and absolute accuracy.

Acknowledgments

This research is supported by the Army Research Office and the Air Force Office of Scientific Research under Grant AFOSR 84-0328. We thank W. P. Allis for his suggestions and insights, and we thank A. C. Gallagher for his help.

References

1. P. Segur, M. Yousfi, J. P. Boeuf, E. Marode, A. J. Davies, and J. G. Evans, in Electrical Breakdown and Discharges in Gases, edited by E. E. Kunhardt and L. H. Luessen, NATO ASI Series B Vol. 89A (Plenum, New York, 1983) p. 331.
2. W. H. Long, Plasma Sheath Processes, Technical Report AFAPL-TR-79-2038, Northrup Research and Technology Center 1978.
3. J. E. Lawler, D. K. Doughty, E. A. Den Hartog, and S. Salih, in Radiative Processes in Discharge Plasmas, ed. by J. M. Proud and L. H. Luessen, NATO ASI Series B Vol. 149 (Plenum, New York, 1986), p. 525.
4. M. Ohuchi and T. Kubota, J. Phys. D: Appl. Phys. 16, 1705 (1983).
5. P. Bayle, J. Vacquie, and M. Bayle, Phys. Rev. A34, 360 (1986) and Phys. Rev. A34, 372 (1986).
6. K. G. Emeleus, J. Phys. D:Appl. Phys. 14, 2179 (1981).
7. K. Kumar, Physics Reports 112, 319 (1984).
8. J. Dutton, J. Phys. Chem. Ref. Data 4, 577 (1975).
9. T. J. Moratz, L. C. Pitchford, and J. N. Bardsley, J. Appl. Phys. 61, 2146 (1987).
10. K. Kitamori, H. Tagashira, and Y. Sakai, J. Phys. D:Appl. Phys. 11, 283 (1978).
11. E. J. Lauer, S. S. Yu, D. M. Cox, Phys. Rev. A23, 2250 (1981).
12. M. A. Folkard and S. C. Haydon, Aust. J. Phys. 24, 527 (1971).
13. J. H. Ingold in Gaseous Electronics ed. by M. N. Hirsh and H. J. Oskam (Academic, New York 1978) Vol. I p. 24.
14. K. G. Muller, Z. Physik 169, 432 (1962).

15. L. Friedland, J. Phys. D:Appl. Phys. 7, 2246 (1974).
16. D. K. Doughty and J. E. Lawler, Appl. Phys. Lett. 45, 611 (1984).
17. J. P. Boeuf and E. Marode, J. Phys. D:Appl. Phys. 15, 2169 (1982).
18. D. K. Doughty and J. E. Lawler, Appl. Phys. Lett. 42, 234 (1983).
19. C. A. Moore, G. P. Davis, R. A. Gottscho, Phys. Rev. Lett. 52, 538 (1984).
20. D. K. Doughty, S. Salih, and J. E. Lawler, Phys. Lett. A103, 41 (1984).
21. R. Warren, Phys. Rev. 98, 1650 (1955).
22. B. N. Ganguly and A. Garscadden, Appl. Phys. Lett. 46, 540 (1985).
23. M. L. Zimmerman, M. G. Littman, M. M. Kash and D. Kleppner, Phys. Rev. A20, 2251 (1979).
24. C. E. Moore, Atomic Energy Levels, U. S. National Bureau of Standards, National Standard Reference Data Series-35 (U.S. GPO, Washington, D. C., 1971).
25. A. R. Edmonds, J. Picart, N. Tran Minh, and R. Pullen, J. Phys. B:Atom. Molec. Phys. 12, 2781 (1979).
26. D. K. Doughty and J. E. Lawler, Phys. Rev. A28, 773 (1983).
27. T. F. Gallagher, S. A. Edelstein, and R. M. Hill, Phys. Rev. A15, 1945 (1977).
28. W. L. Wiese, M. W. Smith, and B. M. Glennon, Atomic Transition Probabilities, Vol. I, Hydrogen Through Neon, U. S. National Bureau of Standards, National Standard Reference Data Series-4 (U. S. GPO, Washington, D. C., 1966).
29. B. N. Ganguly, J. R. Shoemaker, B. L. Preppernau, and A. Garscadden, J. Appl. Phys. 61, 2778 (1987).
30. The pressure-broadening coefficient of  $42.0 \pm 2.7$  MHz/Torr at 292K for the 501.6nm transition is from J. E. Lawler, Ph.D. thesis, University of Wisconsin, 1978 (unpublished).



31. J. E. Lawler, Phys. Rev. A32, 2977 (1985).
32. G. H. Wannier, Statistical Physics (Wiley, New York, 1966), p. 462.
33. F. W. J. Olver, in Handbook of Mathematical Functions, edited by M. Abramowitz and I. A. Stegun (Dover, New York, 1964), p. 376 and 416.
34. M. Abramowitz in Handbook of Mathematical Functions, edited by M. Abramowitz and I. A. Stegun (Dover, New York, 1964), pp. 498 and 501.
35. G. Arfken, Mathematical Methods for Physicists, (Academic Press, New York, 1985), p. 897.
36. H. Helm, J. Phys. B:Atom. Molec. Phys. 10, 3683 (1977).
37. S. Sinha, S. L. Lin, and J. N. Bardsley, J. Phys. B:Atom. Molec. Phys. 12, 1613 (1979).
38. H. F. Wellenstein and W. W. Robertson, J. Chem. Phys. 56, 1072 (1972) and J. Chem. Phys. 56, 1077 (1972).
39. A. V. Phelps, Phys. Rev. 99, 1307 (1955).
40. R. A. Buckingham, and A. Dalgarno, Proc. Roy. Soc. (London) A213, 506 (1952).
41. D. C. Allison, J. C. Browne, and A. Dalgarno, Proc. Phys. Soc. (London) 89, 41 (1966).
42. R. W. LaBahn and J. Callaway, Phys. Rev. A2, 366 (1970), Phys. Rev. 180, 91 (1969), Phys. Rev. 188, 520 (1969).
43. G. D. Alkhazov, Zh.Tekh. Fiz. 40, 97 (1970) [Sov. Phys. Tech. Phys. 15, 66 (1970)].
44. D. A. Doughty, E. A. Den Hartog, and J. E. Lawler, Phys. Rev. Lett. 58, 2668 (1987).
45. A. V. Phelps and L. C. Pitchford, Phys. Rev. A31, 2932 (1985).

46. R. D. Rundel, F. B. Dunning, J. S. Howard, J. P. Riola, and  
R. F. Stebbings, Rev. Sci. Instrum. 44, 60 (1973).
47. W. C. Fon, K. A. Berrington, P. G. Burke, and A. E. Kingston,  
J. Phys. B:At. Mol. Phys. 14, 2921 (1981).
48. R. Deloche, P. Monchicourt, M. Cheret, and F. Lambert, Phys. Rev. A13, 1140  
(1974).

Figure Captions

- Fig. 1 Schematic of the experimental apparatus showing all three detection methods: optogalvanic, fluorescence, and absorption detection.
- Fig. 2 (a) Theoretical Stark map for the  $n=11$  singlet  $m=0$  levels of He.  
(b) Theoretical intensities of selected Stark components as a function of electric field.
- Fig. 3 Optogalvanic Stark spectra in the 3.50 Torr He discharge operating at  $1.50\text{mA}/\text{cm}^2$ . The distance from the cathode in cm at which each spectra is taken is indicated at the right.
- Fig. 4 Electric field as a function of distance from the cathode for five current densities, all at 3.50 Torr. The lines are linear-least-square fits to the data. The anode corresponds to the right-hand side of the figure.
- Fig. 5 Experimentally derived gas density as a function of discharge power measured at a constant pressure of 3.50 Torr.
- Fig. 6 Integrals of the Eq. 6 distribution function verses the number of mean-free-paths from the source at  $z_0$  near the origin: (a) flux density, (b) average velocity, (c) ratio of average velocity to local equilibrium drift velocity, (d) density.
- Fig. 7 Helium  $2^1\text{S}$  metastable density as a function of distance from the cathode for five discharge current densities at 3.50 Torr.
- Fig. 8 Helium  $2^3\text{S}$  metastable density as a function of distance from the cathode for five discharge current densities at 3.50 Torr.
- Fig. 9 Helium  $2^1\text{S}$  metastable density for  $J_D = 1.18\text{mA}/\text{cm}^2$ . The points are the experimental data and the dashed curve is the calculated fit to the data.

Fig. 10 Helium  $2^3S$  metastable density for  $J_D = 1.18 \text{ mA/cm}^2$ . The points are the experimental data and the dashed curve is the calculated fit to the data.

Fig. 11 Monte Carlo histograms showing the number of a) excitation events and b) ionization events per (net) electron emitted from the cathode as a function of distance from the cathode. The histogram for total excitation is subdivided into  $2^1S$ ,  $2^3S$  and  $2^1P$  excitation. The histogram for total ionization is subdivided into associative and direct ionization.

Fig. 12 Ratio of ion current to electron current at the cathode surface  $J_+^0/(J_D - J_+^0)$  as a function of discharge current density. The points are the empirically derived values; the dashed line is the Monte Carlo results assuming the isotropic scattering for ionizing collisions; the solid line is the Monte Carlo results incorporating the anisotropic scattering for ionizing collisions.

Fig. 13 (a) Helium  $2^1S$  production, (b) Helium  $2^3S$  production and (c) total metastable production as a function of discharge current density. The production values presented are spatially averaged production per (net) electron released from the cathode. The points are empirical results with error bars reflecting only the uncertainty of the metastable density measurements. The solid lines are Monte Carlo results using the anisotropic angular distributions for ionizing collisions.

Fig. 14 Negative glow electron density versus electron temperature for five discharge current densities. The bold line is the relationship from the analysis of the metastable maps. The light solid line is from the ambipolar-like diffusion of the electron ion pairs in the negative glow.

The intersection of the two lines determines the density and temperature of the low energy electrons in the negative glow.

Table I. Summary of the analysis of the electric field and gas density measurements to determine the current balance at the cathode surface. The dimensionless ratio  $J_+^0/(J_D - J_+^0)$  is the number of ions produced in the cathode fall region per (net) electron emitted from the cathode.

$J_D$ (mA/cm <sup>2</sup> )	0.190	0.519	0.846	1.18	1.50
$E^0$ (kV/cm)	0.897	1.426	1.870	2.395	3.017
$d_c$ (cm)	0.382	0.301	0.282	0.300	0.396
$V_{vm}$ (kV)	0.173	0.211	0.261	0.356	0.600
$V_{ef}$ (kV)	0.171	0.215	0.264	0.359	0.597
$N$ (10 <sup>16</sup> cm <sup>-3</sup> )	11.2	10.8	10.3	9.48	8.01
$\rho_+$ (10 <sup>-10</sup> C/cm <sup>3</sup> )	2.08	4.20	5.88	7.07	6.74
$\langle m_+ v_z^2/2 \rangle^0$ (eV)	1.66	2.82	3.89	5.71	8.92
$\sigma$ (10 <sup>-16</sup> cm <sup>2</sup> )	-	-	23.3	22.1	21.1
$\langle v_z \rangle^0$ (10 <sup>5</sup> cm/s)	7.12	9.28	10.9	13.2	16.5
$J_+^0$ (mA/cm <sup>2</sup> )	0.148	0.390	0.641	0.933	1.11
$J_+^0/(J_D - J_+^0)$	3.52	3.02	3.13	3.78	2.85

Table II. Summary for all current densities of parameters used in the model as well as the key quantities  $\int P_s dz$ ,  $\int P_t dz$  and  $\kappa n_e$ . The dimensionless ratios  $e\int P_s dz/(J_D - J_+^0)$  and  $e\int P_t dz/(J_D - J_+^0)$  are the average number of singlet and triplet metastables produced per (net) electron emitted from the cathode.

$J_D$ (mA/cm <sup>2</sup> )	0.190	0.519	0.846	1.18	1.50
$N$ (10 <sup>16</sup> cm <sup>-3</sup> )	11.2	10.8	10.3	9.48	8.01
$D_s$ (cm <sup>2</sup> /s)	127	140	152	173	236
$D_t$ (cm <sup>2</sup> /s)	136	150	163	185	253
$\gamma$ (10 <sup>-15</sup> cm <sup>3</sup> /s)	6.0	6.5	6.9	7.8	9.9
$\beta$ (10 <sup>-9</sup> cm <sup>3</sup> /s)	3.5	3.5	3.5	3.5	3.5
$\int P_s dz$ (10 <sup>15</sup> cm <sup>-2</sup> s <sup>-1</sup> )	0.454	0.664	0.830	1.05	1.38
$\int P_t dz$ (10 <sup>15</sup> cm <sup>-2</sup> s <sup>-1</sup> )	0.711	1.86	2.77	3.56	4.34
$e\int P_s dz/(J_D - J_+^0)$	1.73	0.824	0.648	0.680	0.566
$e\int P_t dz/(J_D - J_+^0)$	2.71	2.31	2.16	2.31	1.78
$\kappa n_e$ (10 <sup>4</sup> s <sup>-1</sup> )	1.5	8.5	7.0	5.5	3.0

Table III. Results of Monte Carlo simulations of electron avalanches based on the isotropic angular distribution for ionizing collisions. All results are per (net) electron emitted from the cathode. The ionization in the cathode fall region includes direct plus associative ionization occurring between the surface of the cathode and a distance  $d_c$  from the cathode. Other quantities include all events between the cathode and anode.

$J_D$ (mA/cm <sup>2</sup> )	0.190	0.519	0.846	1.18	1.50
$E^0$ (kV/cm)	0.897	1.426	1.870	2.395	3.017
$d_c$ (cm)	0.382	0.301	0.282	0.300	0.396
$N$ (10 <sup>16</sup> cm <sup>-3</sup> )	11.2	10.8	10.3	9.48	8.01
2 <sup>1</sup> S production	0.88	0.88	0.99	1.06	0.96
2 <sup>3</sup> S production	2.05	1.92	2.04	2.04	1.62
2 <sup>1</sup> P production	3.06	3.37	3.91	4.50	4.51
Associative ionization	0.36	0.38	0.42	0.47	0.49
Direct ionization	4.70	5.98	7.31	9.02	9.84
Ionization in the cathode fall region	3.89	3.77	4.06	4.52	5.71



Table IV. Results of Monte Carlo simulations of electron avalanches based on the anisotropic angular distribution for ionizing collisions. The quantity  $\langle T_{an} \rangle$  is the average kinetic energy of electrons hitting the anode. Other quantities are per (net) electron emitted from the cathode.

$J_D$ (mA/cm <sup>2</sup> )	0.190	0.519	0.846	1.18	1.50
$E^0$ (kV/cm)	0.897	1.426	1.870	2.395	3.017
$d_c$ (cm)	0.382	0.301	0.282	0.300	0.396
$N$ (10 <sup>16</sup> cm <sup>-3</sup> )	11.2	10.8	10.3	9.48	8.01
2 <sup>1</sup> S production	0.77	0.75	0.75	0.74	0.53
2 <sup>3</sup> S production	1.79	1.58	1.52	1.40	0.83
2 <sup>1</sup> P production	2.82	2.98	3.14	3.28	2.51
Associative ionization	0.29	0.31	0.32	0.34	0.25
Direct ionization	4.37	5.37	6.13	6.88	5.86
$\langle T_{an} \rangle$ (eV)	14.0	16.7	21.8	36.5	106.5
Ionization in the cathode fall region	3.40	3.10	2.97	3.11	3.24

Table V. Power balance comparison between the results of Monte Carlo simulations and the empirical input power. The variable H is the sum of  $H_{it}$ ,  $H_{ion}$ ,  $H_{exc}$ , and  $H_{an}$ .

$J_D$ (mA/cm <sup>2</sup> )	0.190	0.519	0.846	1.18	1.50
$H_{it}$ (mW/cm <sup>2</sup> )	20.3	66	132	254	550
$H_{ion}$ (mW/cm <sup>2</sup> )	4.7	17	33	49	52
$H_{exc}$ (mW/cm <sup>2</sup> )	5.1	15	26	35	31
$H_{an}$ (mW/cm <sup>2</sup> )	3.4	14	35	86	268
H (mW/cm <sup>2</sup> )	33.5	112	226	424	901
$V_{vm}J_D$ (mW/cm <sup>2</sup> )	32.9	110	221	420	900

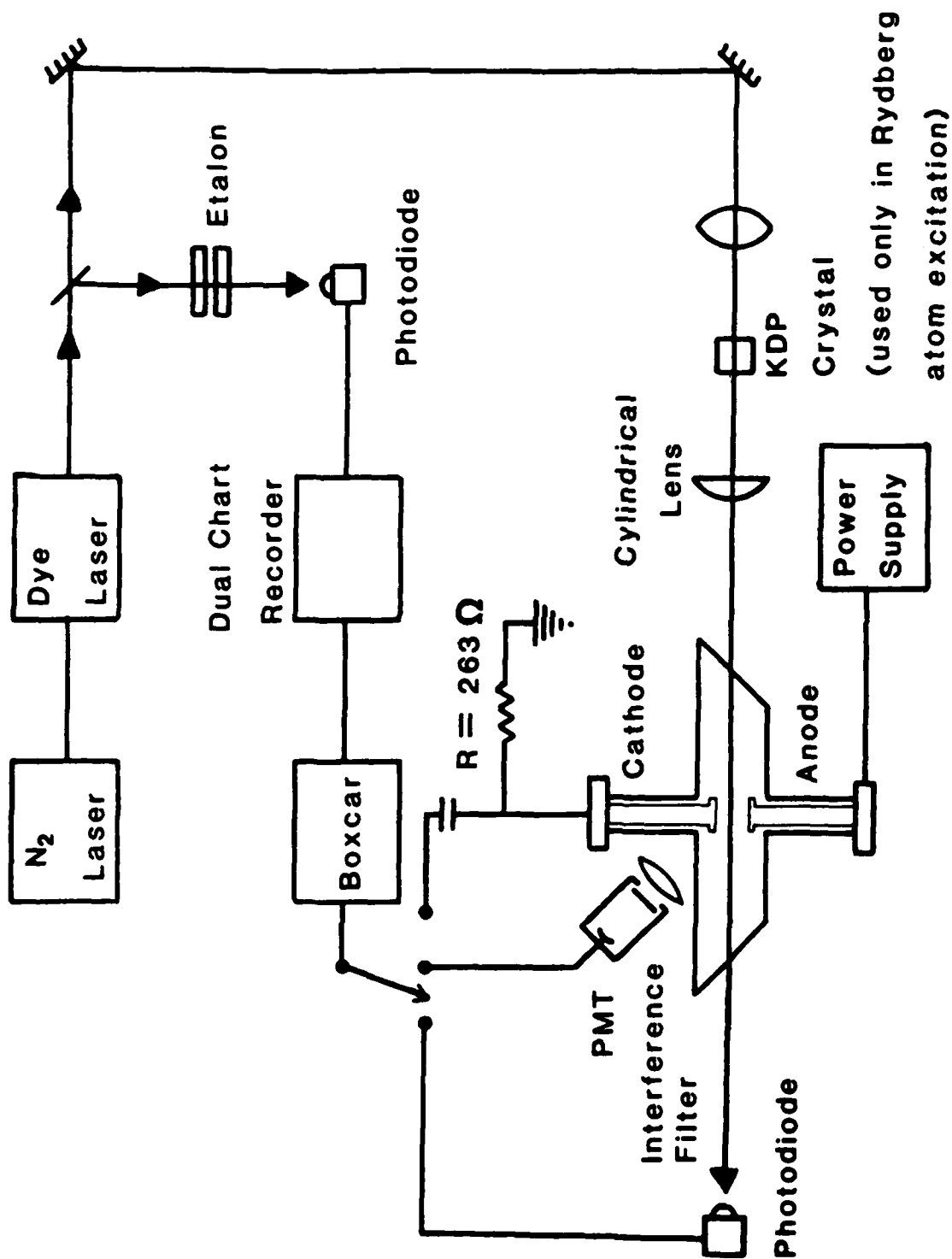


Fig. 1 Schematic of the experimental apparatus showing all three detection methods: optogalvanic, fluorescence, and absorption detection.

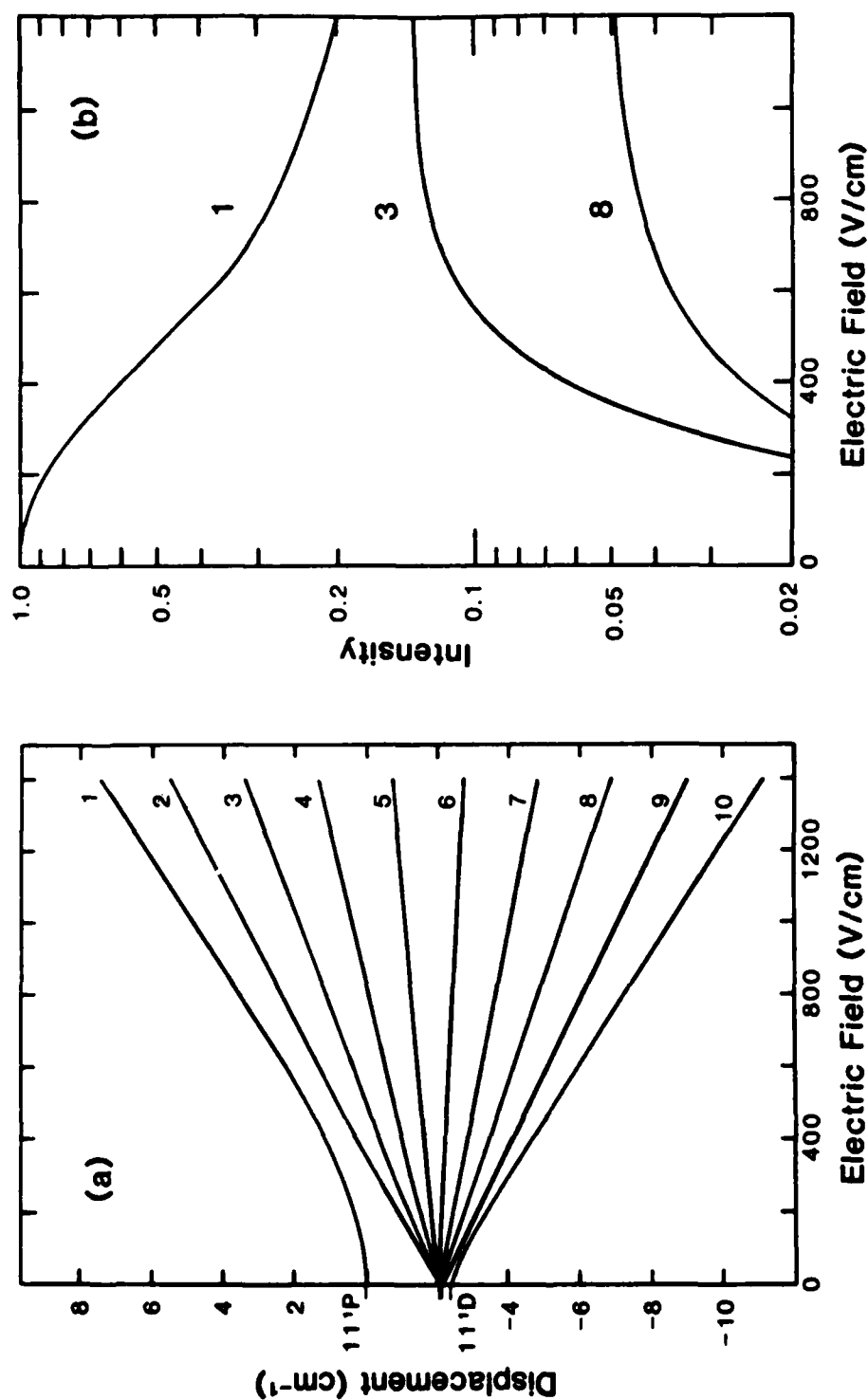
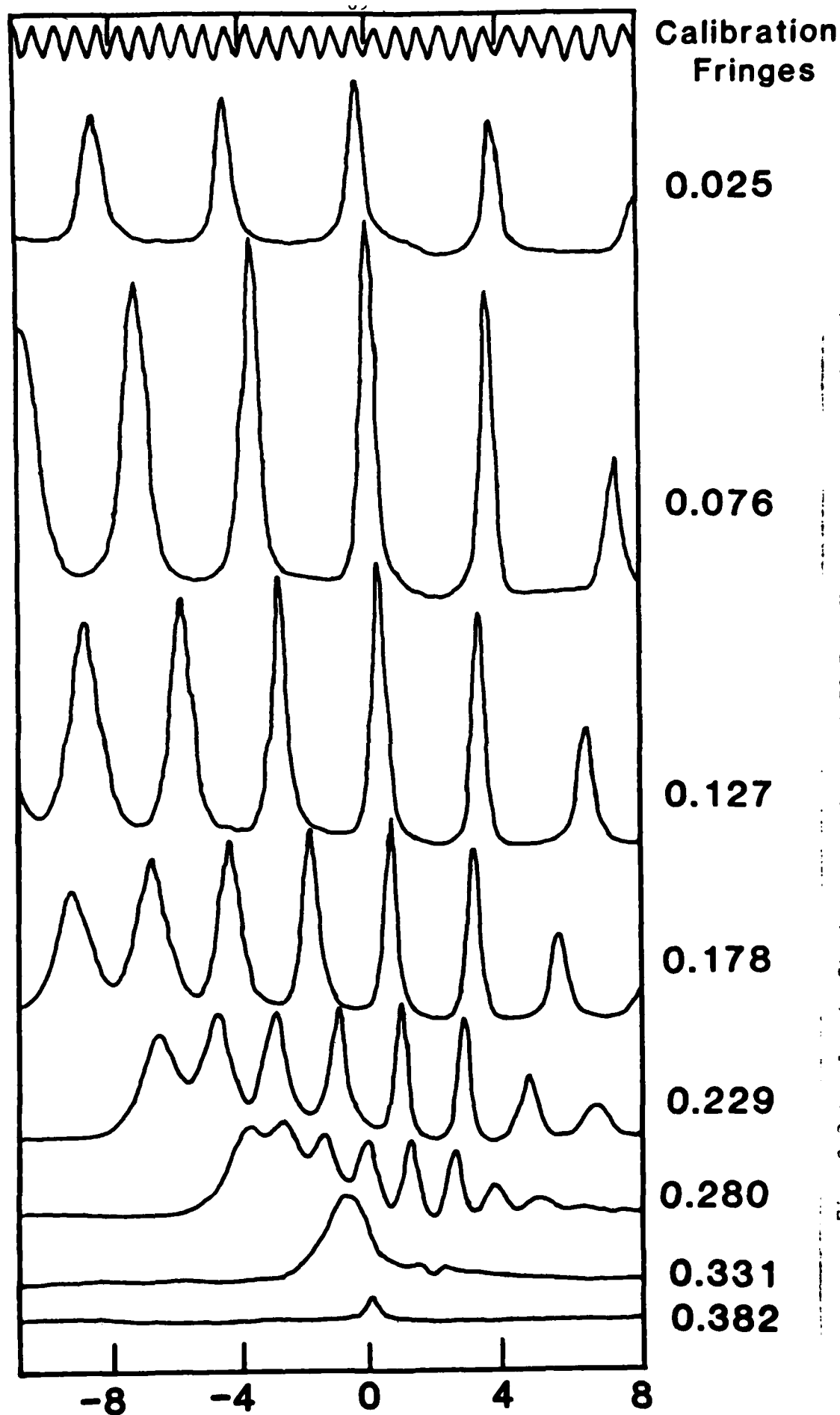


Fig. 2 (a) Theoretical Stark map for the  $n=11$  singlet  $m=0$  levels of He.  
 (b) Theoretical intensities of selected Stark components as a function of electric field.

# **OPTOGALVANIC SIGNAL**



**LASER FREQUENCY OFFSET ( $\text{cm}^{-1}$ )**

Fig. 3 Optogalvanic Stark spectra in the 3.50 Torr He discharge operating at 1.50mA/cm<sup>2</sup>. The distance from the cathode in cm at which each spectra is taken is indicated at the right.

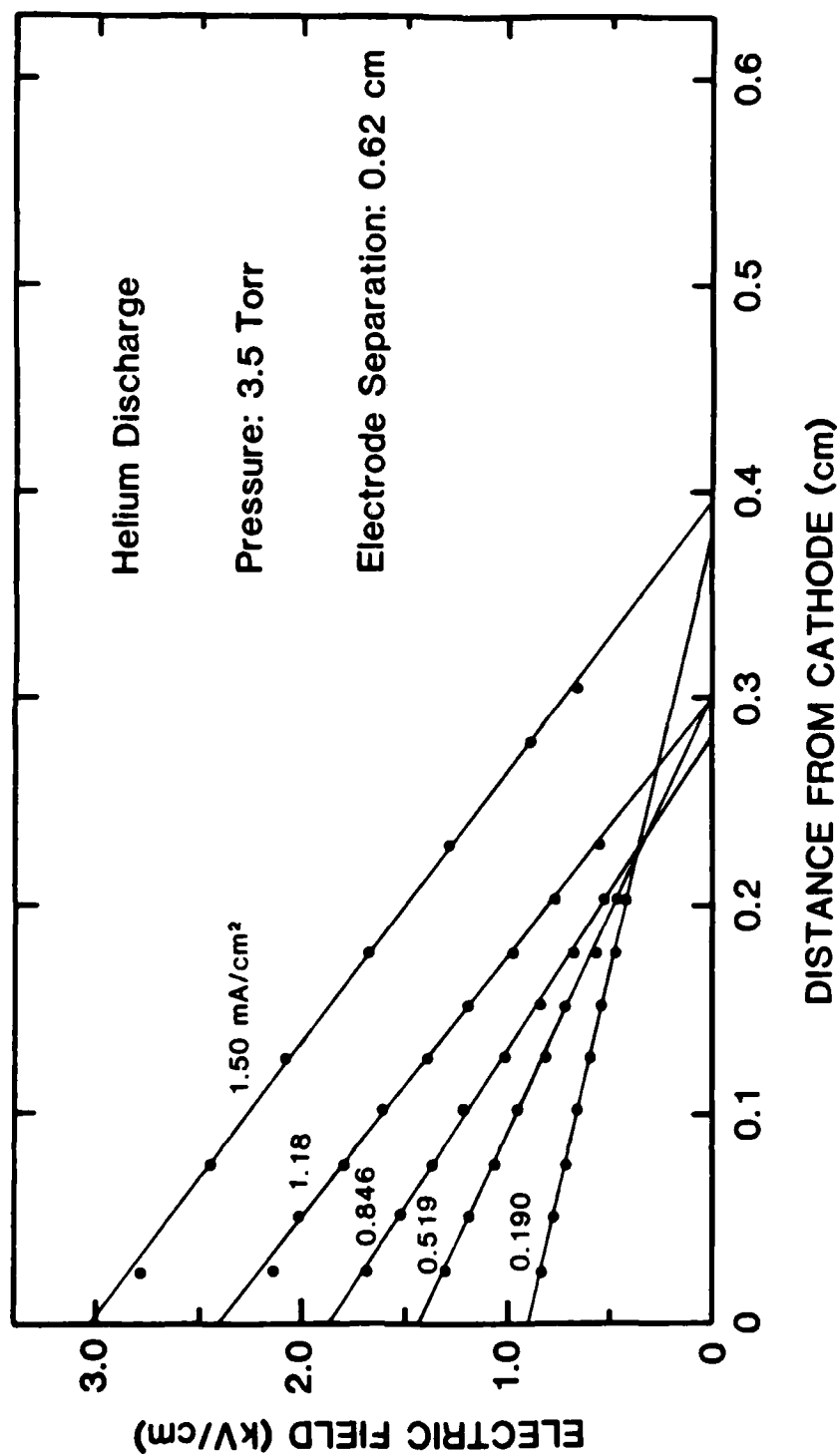


Fig. 4 Electric field as a function of distance from the cathode for five current densities, all at 3.50 Torr. The lines are linear-least-square fits to the data. The anode corresponds to the right-hand side of the figure.

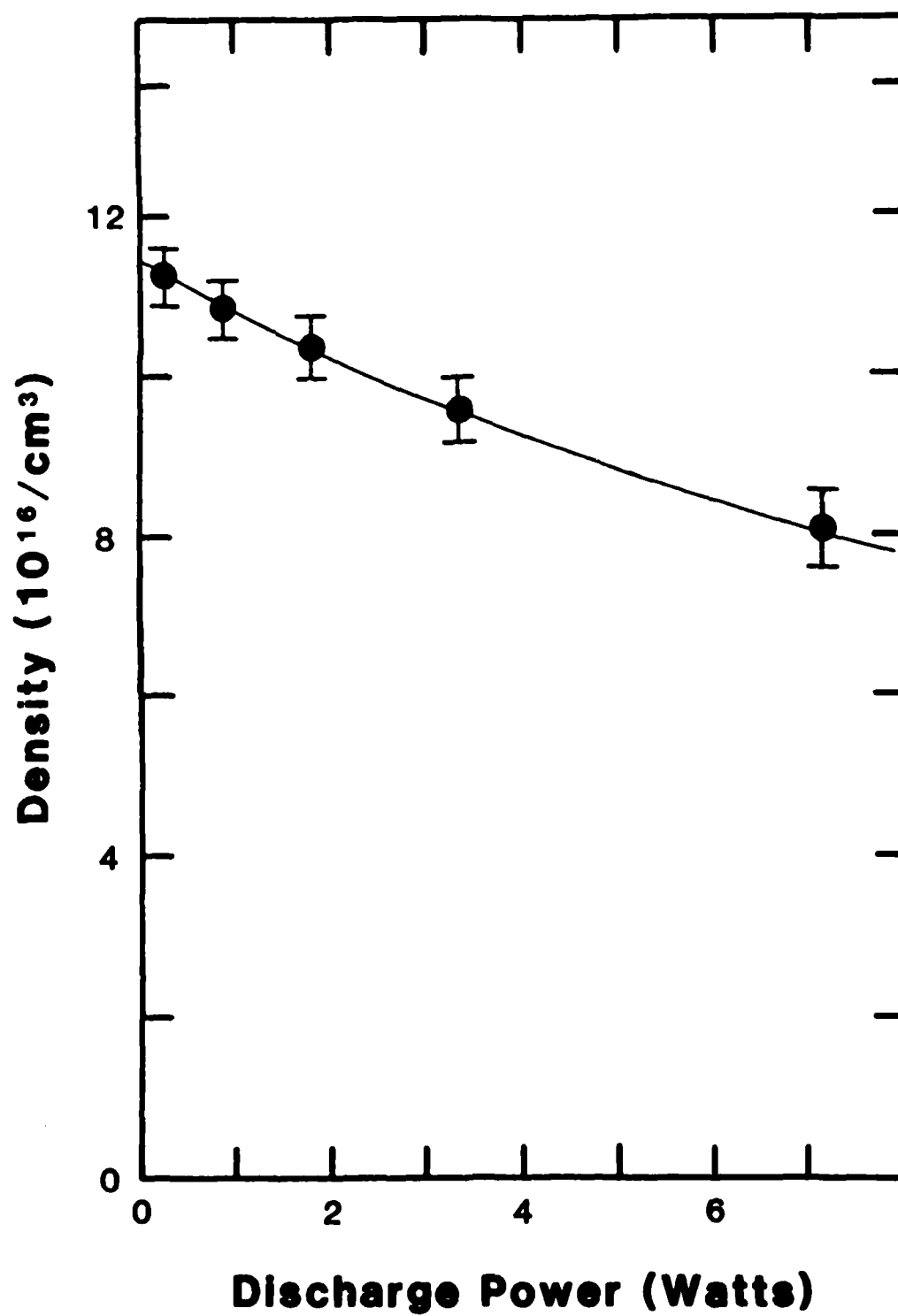


Fig. 5 Experimentally derived gas density as a function of discharge power  
measured at a constant pressure of 3.50 Torr.

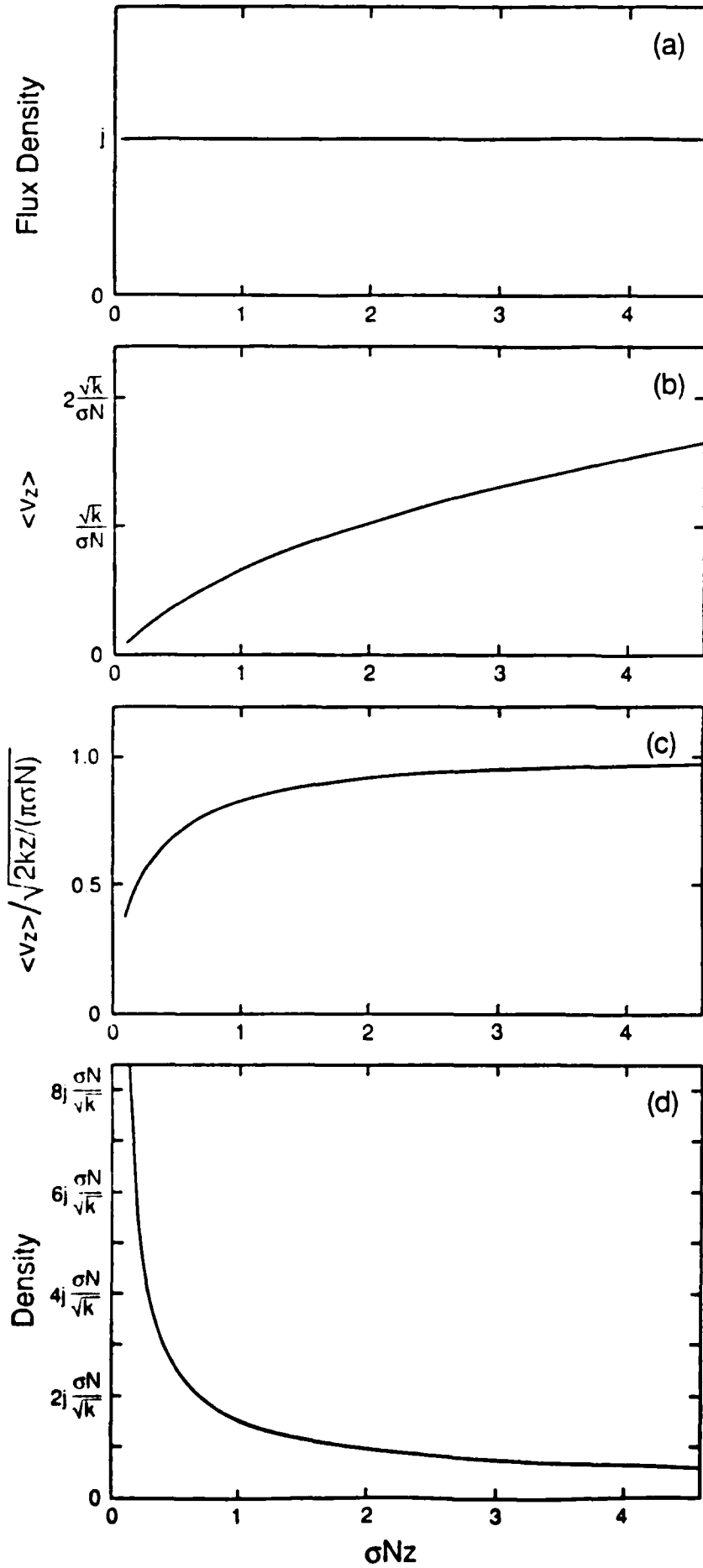


Fig. 6 Integrals of the Eq. 6 distribution function verses the number of mean-free-paths from the source at  $z_0$  near the origin: (a) flux density, (b) average velocity, (c) ratio of average velocity to local equilibrium drift velocity, (d) density.



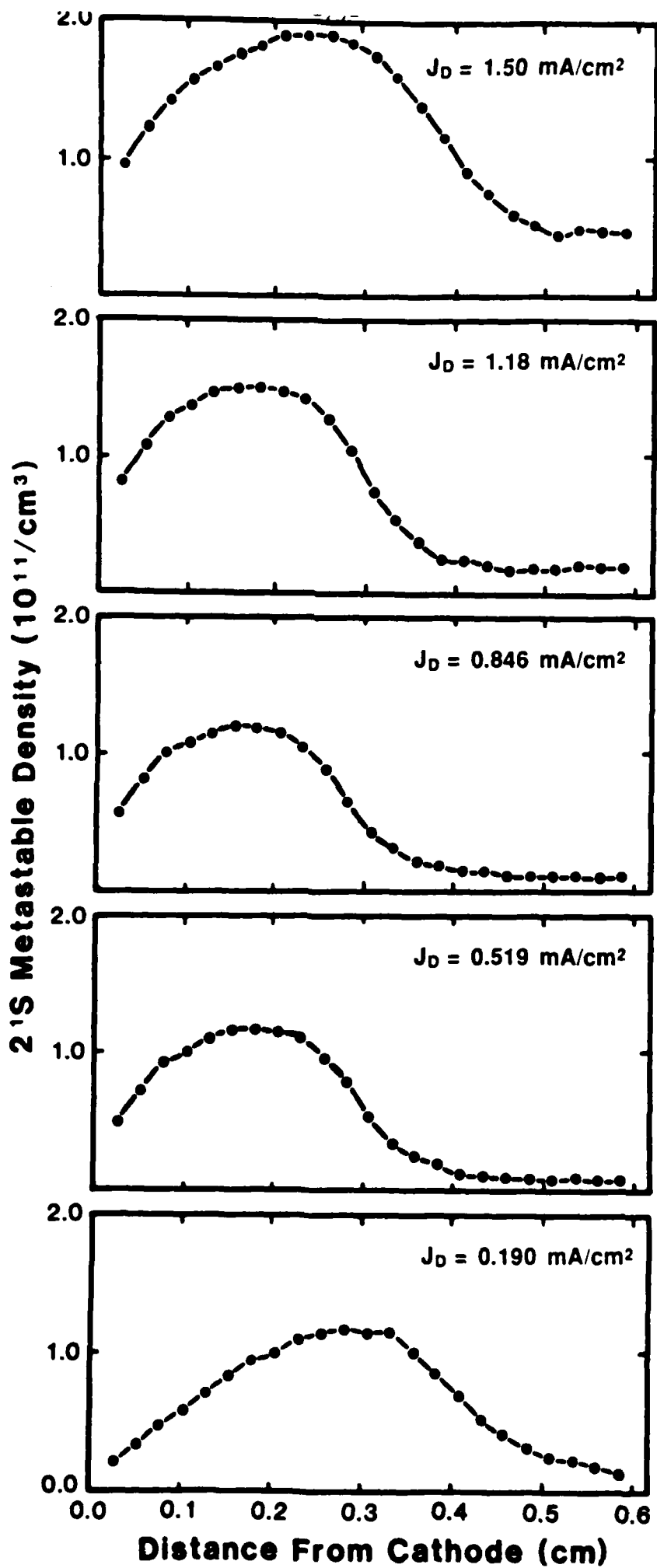


Fig. 7 Helium  $2^1S$  metastable density as a function of distance from the cathode for five discharge current densities at 3.50 Torr.

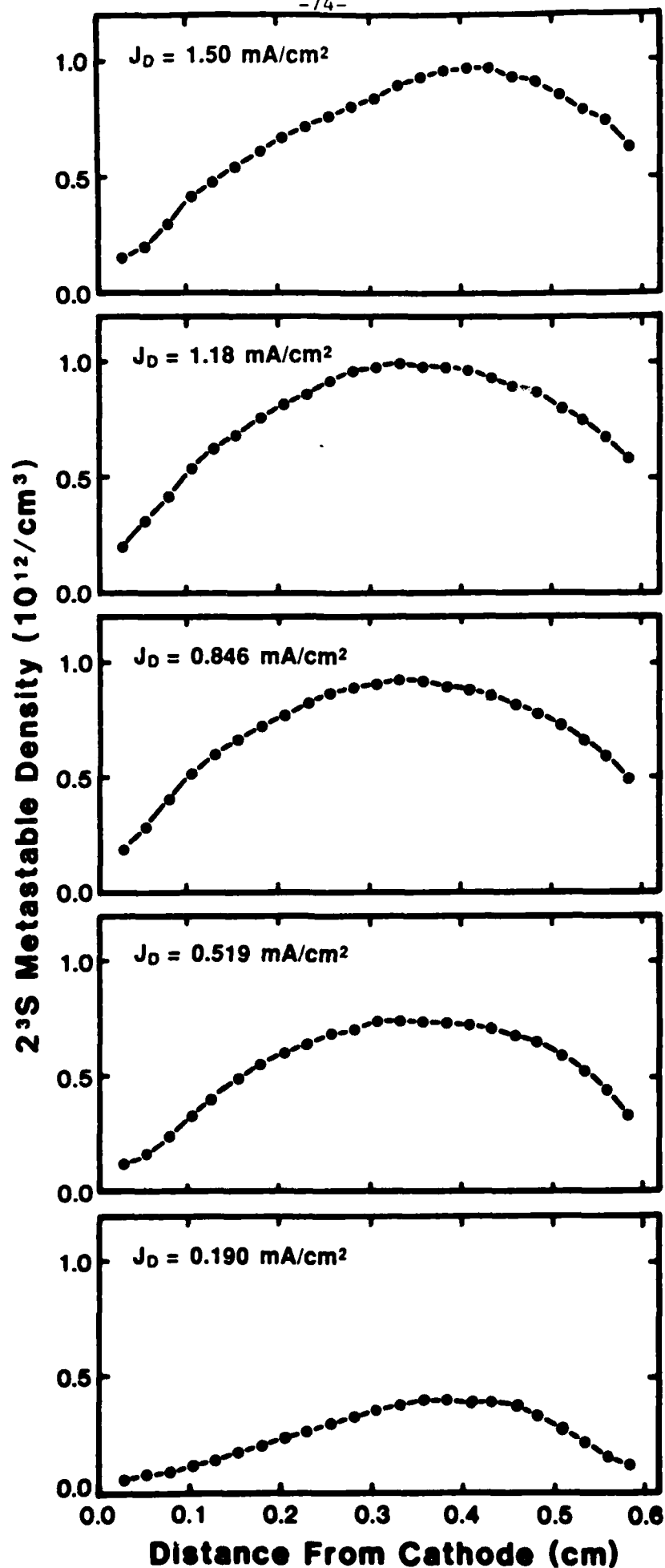


Fig. 8 Helium  $2^3S$  metastable density as a function of distance from the cathode for five discharge current densities at 3.50 Torr.

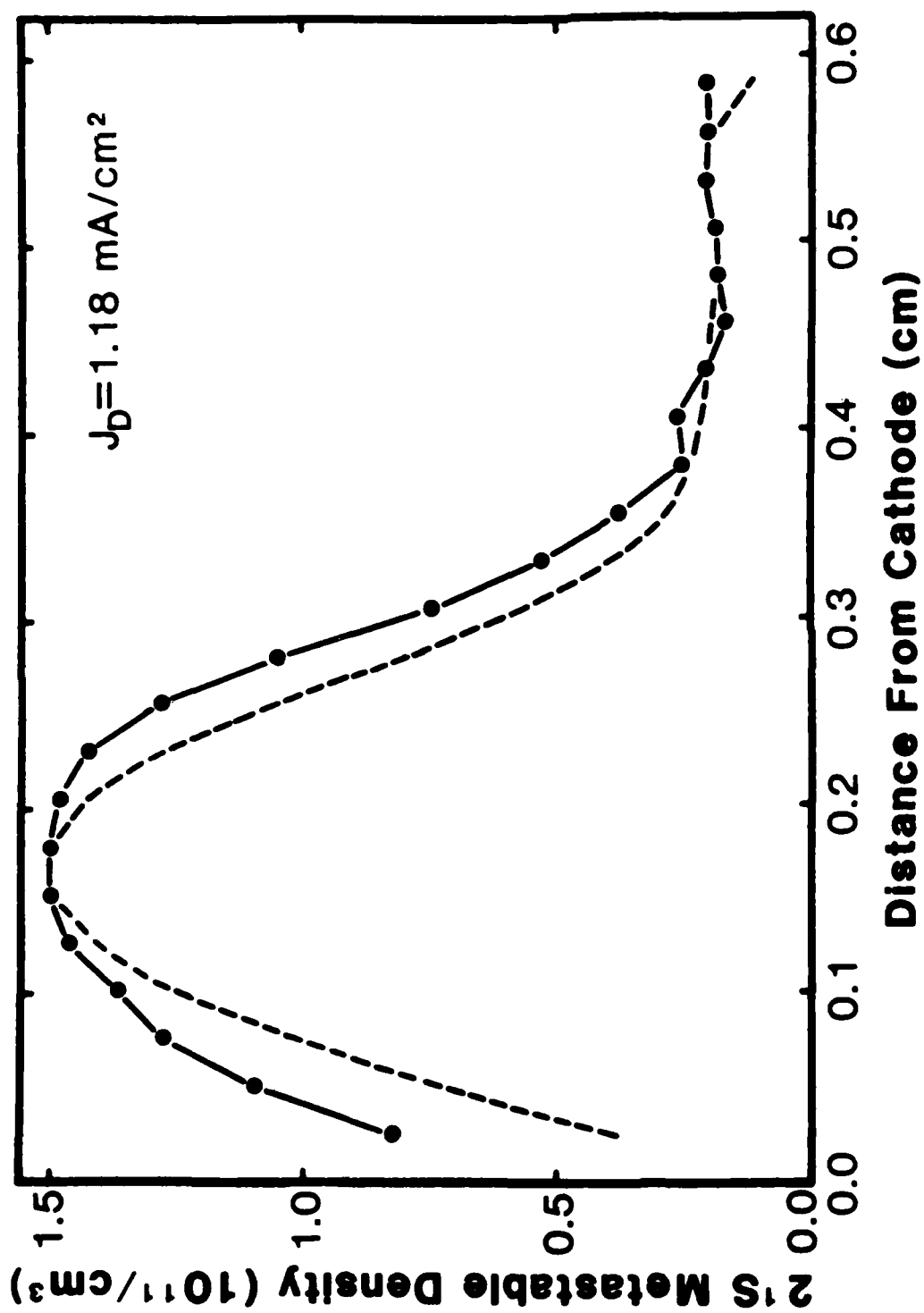


Fig. 9 Helium  $2^1\text{S}$  metastable density for  $J_D = 1.18 \text{ mA/cm}^2$ . The points are the experimental data and the dashed curve is the calculated fit to the data.

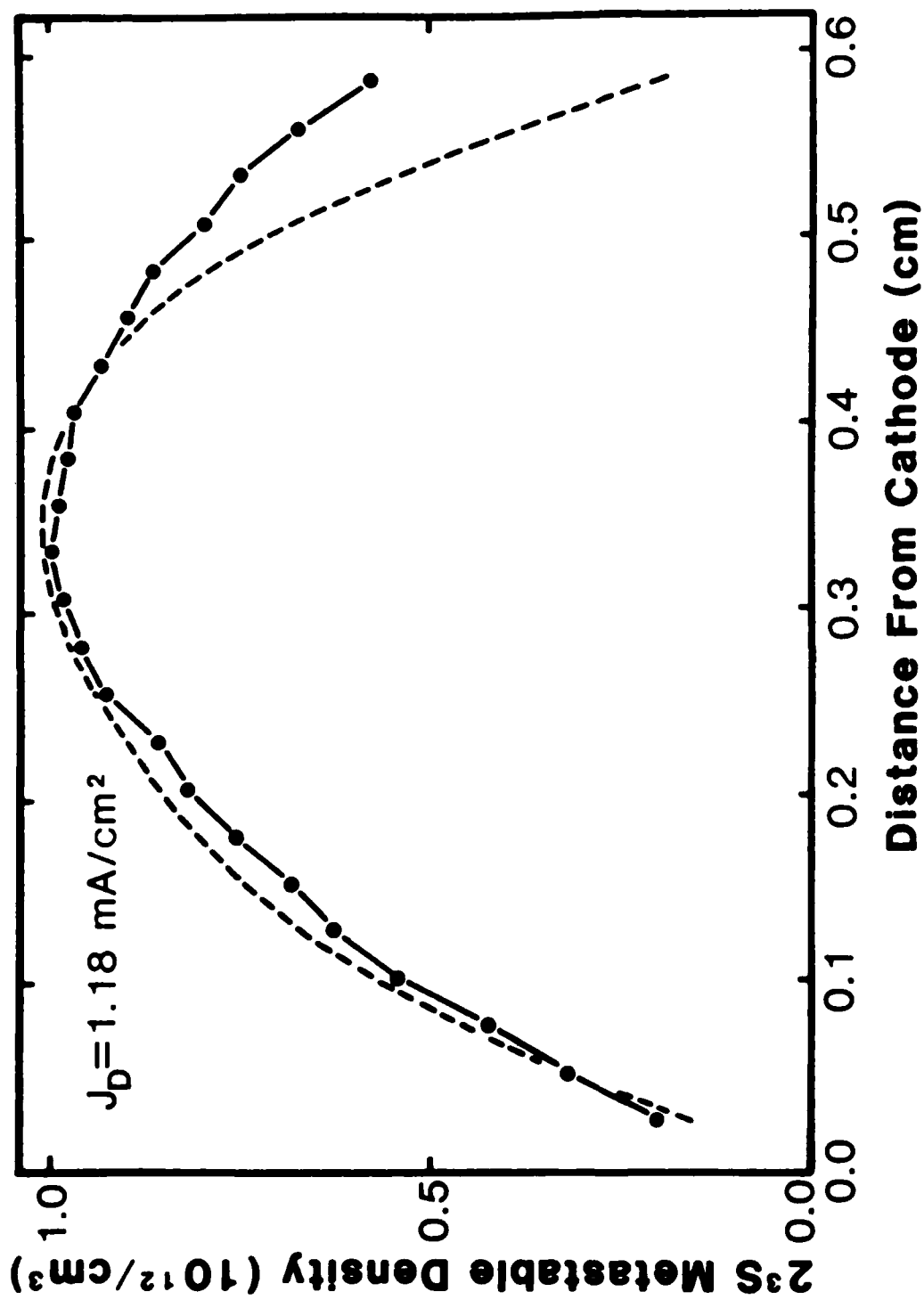


Fig. 10 Helium  $^{23}\text{S}$  metastable density for  $J_D = 1.18 \text{ mA/cm}^2$ . The points are the experimental data and the dashed curve is the calculated fit to the data.

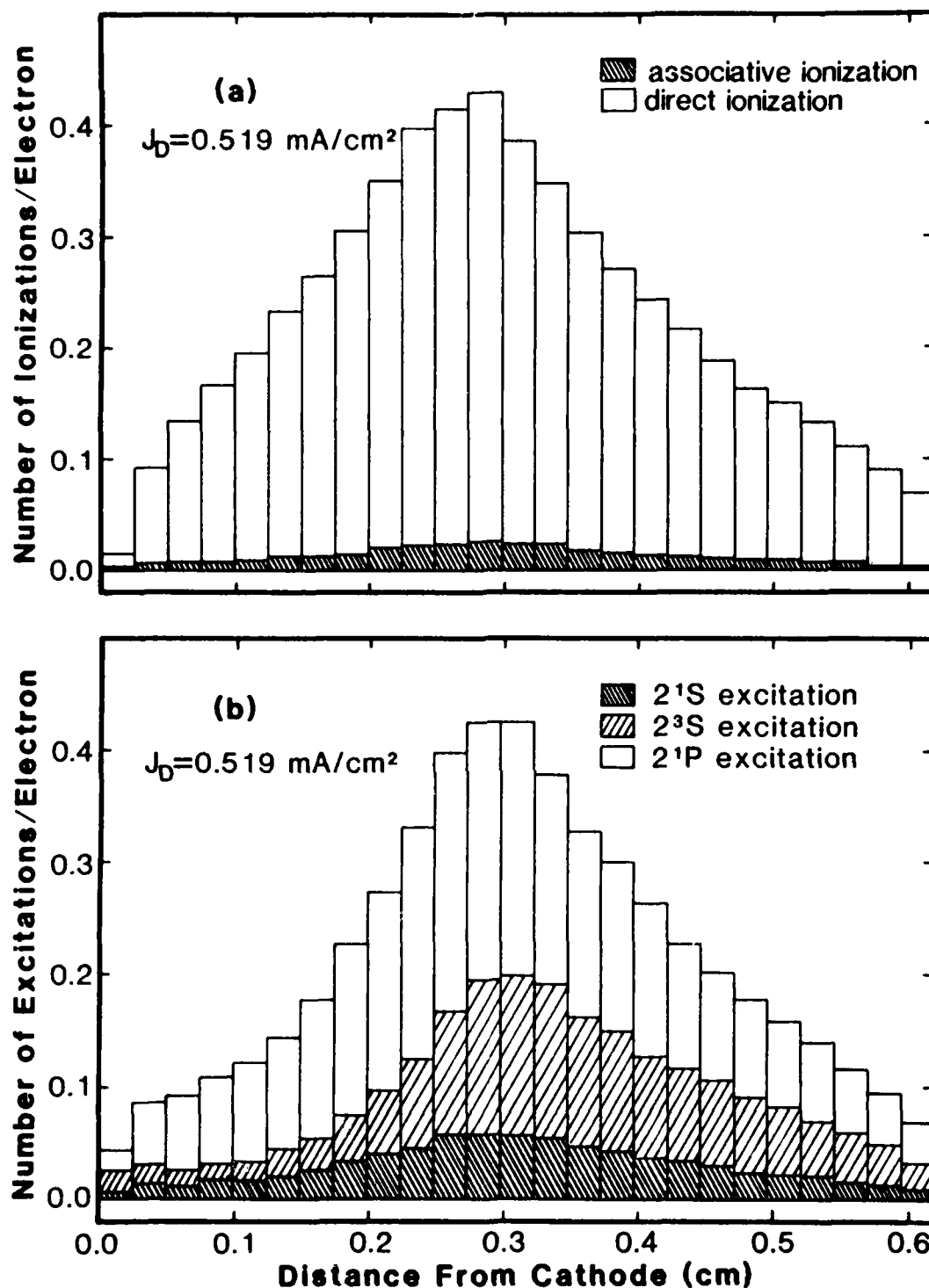


Fig. 11 Monte Carlo histograms showing the number of a) excitation events and b) ionization events per (net) electron emitted from the cathode as a function of distance from the cathode. The histogram for total excitation is subdivided into  $2^1S$ ,  $2^3S$  and  $2^1P$  excitation. The histogram for total ionization is subdivided into associative and direct ionization.

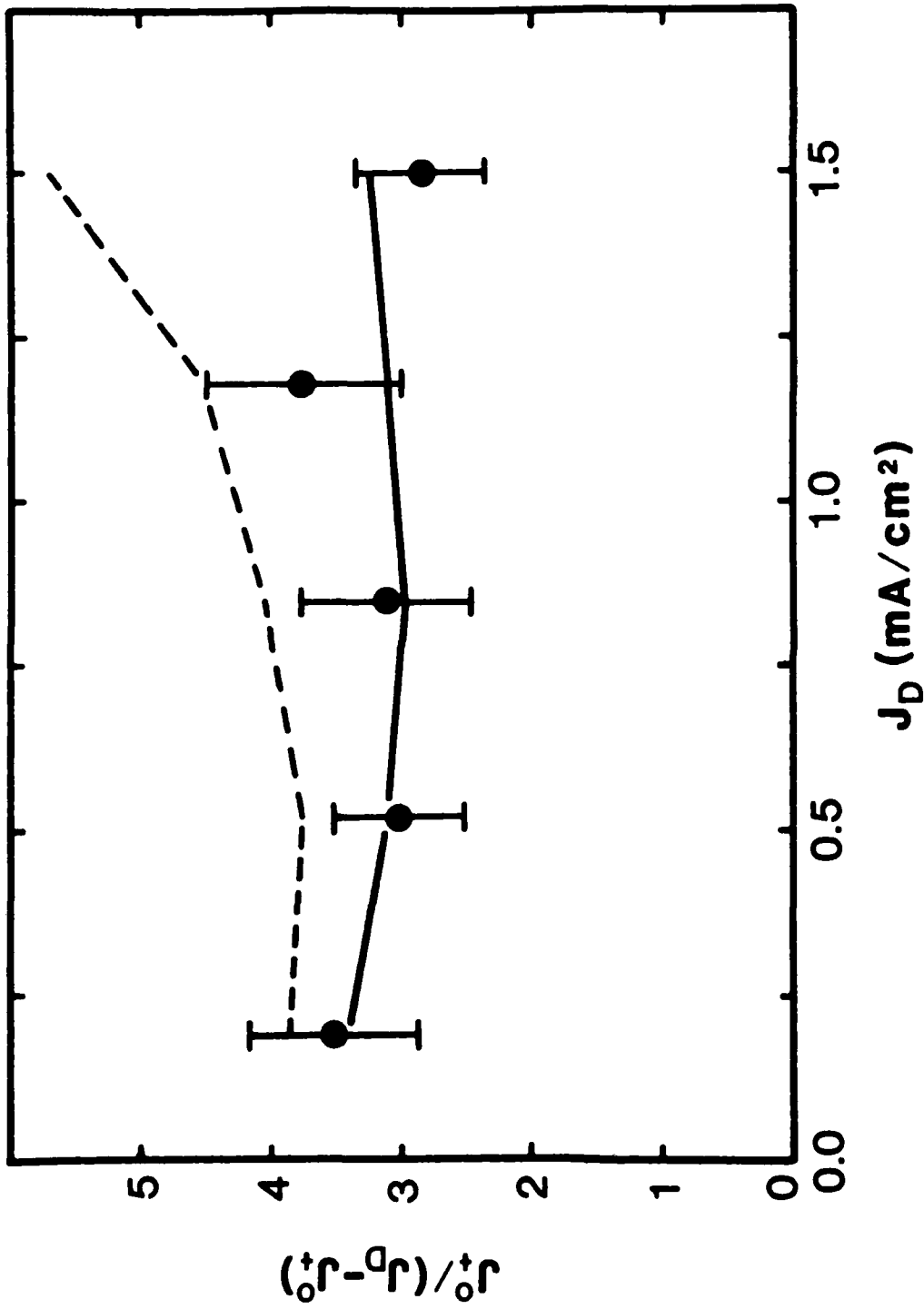


Fig. 12 Ratio of ion current to electron current at the cathode surface  $j_0^+/(j_D - j_0^0)$  as a function of discharge current density. The points are the empirically derived values; the dashed line is the Monte Carlo results assuming the isotropic scattering for ionizing collisions; the solid line is the Monte Carlo results incorporating the anisotropic scattering for ionizing collisions.

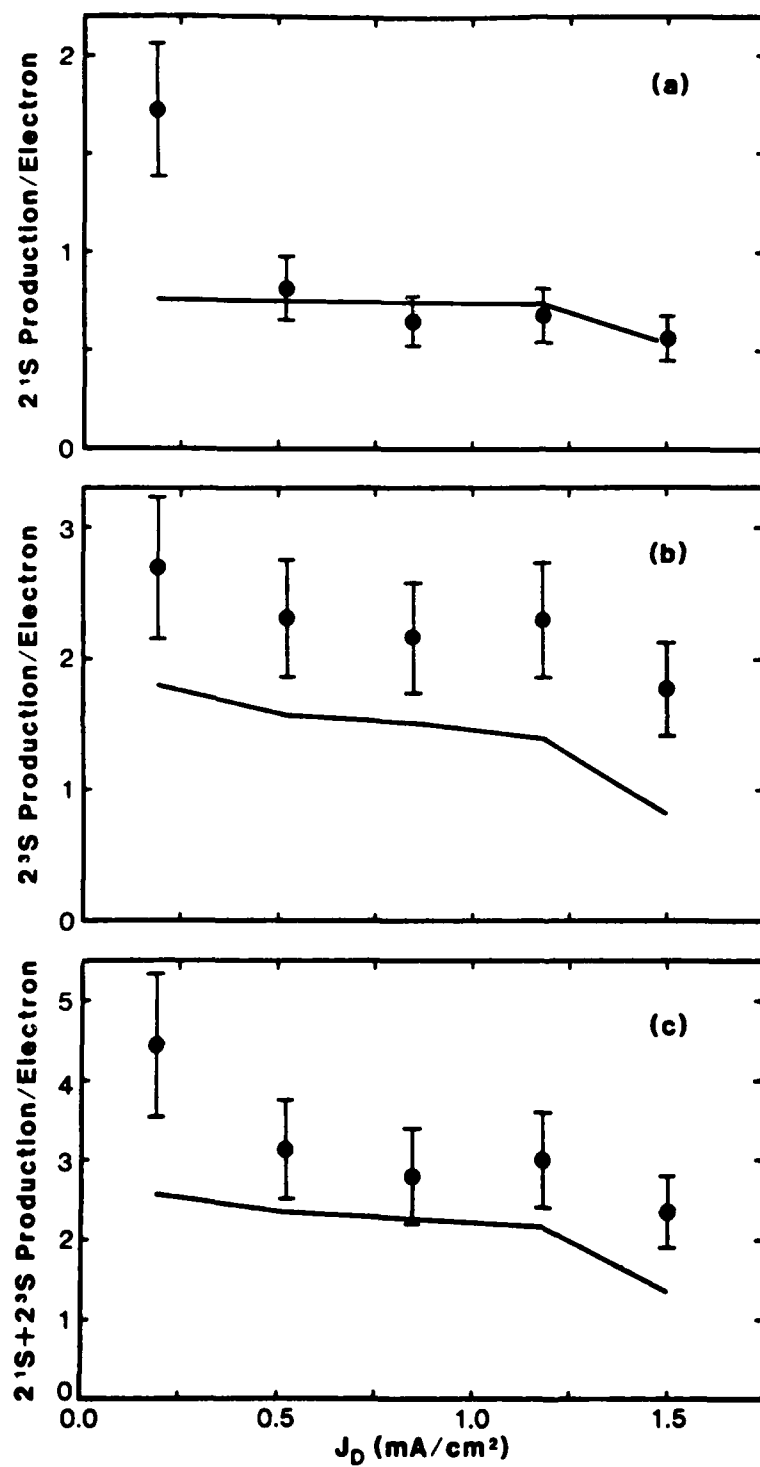


Fig. 13 (a) Helium  $2^1S$  production, (b) Helium  $2^3S$  production and (c) total metastable production as a function of discharge current density. The production values presented are spatially averaged production per (net) electron released from the cathode. The points are empirical results with error bars reflecting only the uncertainty of the metastable density measurements. The solid lines are Monte Carlo results using the anisotropic angular distributions for ionizing collisions.

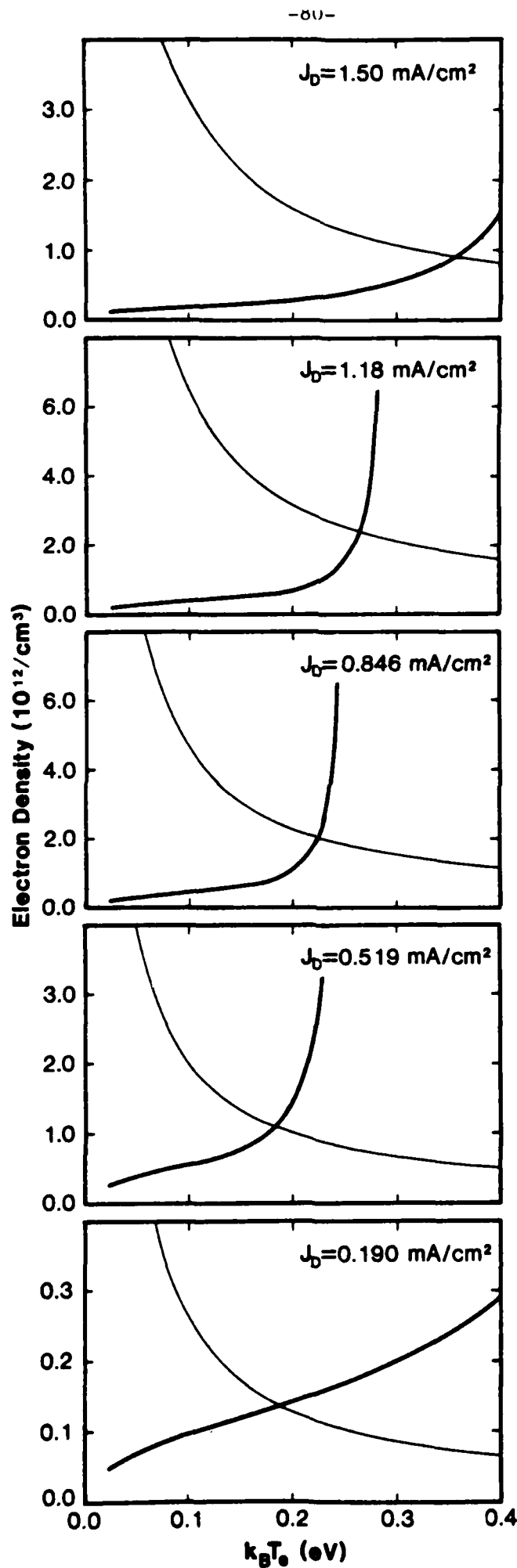


Fig. 14 Negative glow electron density versus electron temperature for five discharge current densities. The bold line is the relationship from the analysis of the metastable maps. The light solid line is from the ambipolar-like diffusion of the electron ion pairs in the negative glow. The intersection of the two lines determines the density and temperature of the low energy electrons in the negative glow.



END

DATE

FILMED

3-88

DTIC